nature COMMUNICATIONS

ARTICLE

Received 16 Feb 2016 | Accepted 1 Jul 2016 | Published 16 Aug 2016

DOI: 10.1038/ncomms12442 OPEN

Blocking transport resonances via Kondo many-body entanglement in quantum dots

Michael Niklas[1], Sergey Smirnov[1], Davide Mantelli[1], Magdalena Margańska[1], Ngoc-Viet Nguyen[2], Wolfgang Wernsdorfer[2], Jean-Pierre Cleuziou[2,3] & Milena Grifoni[1]

Many-body entanglement is at the heart of the Kondo effect, which has its hallmark in quantum dots as a zero-bias conductance peak at low temperatures. It signals the emergence of a conducting singlet state formed by a localized dot degree of freedom and conduction electrons. Carbon nanotubes offer the possibility to study the emergence of the Kondo entanglement by tuning many-body correlations with a gate voltage. Here we show another side of Kondo correlations, which counterintuitively tend to block conduction channels: inelastic co-tunnelling lines in the magnetospectrum of a carbon nanotube strikingly disappear when tuning the gate voltage. Considering the global $SU(2) \otimes SU(2)$ symmetry of a nanotube coupled to leads, we find that only resonances involving flips of the Kramers pseudospins, associated to this symmetry, are observed at temperatures and voltages below the corresponding Kondo scale. Our results demonstrate the robust formation of entangled many-body states with no net pseudospin.

[1] Institute for Theoretical Physics, University of Regensburg, 93040 Regensburg, Germany. [2] Institut Néel, CNRS and Université Grenoble Alpes, 38042 Grenoble, France. [3] INAC-SPSMS, CEA and Université Grenoble Alpes, 38054 Grenoble, France. Correspondence and requests for materials should be addressed to M.G. (email: milena.grifoni@ur.de).

The ubiquity of Kondo resonances in quantum dots relies on the fact that their occurrence requires only the presence of degenerate dot states, whose degeneracy is associated with degrees of freedom that are conserved during the tunnelling on and out of the dot[1]. Finite magnetic fields can be used to break time-reversal symmetry-related degeneracies and unravel the deep nature of the Kondo state by tracking the magnetic field evolution of split Kondo peaks[2–11]. In a recent work[12], the striking report was made that specific transport resonances were not observable in nonlinear magnetoconductance measurements of split Kondo peaks in carbon nanotubes (CNTs), despite being expected from theoretical predictions[13–15]. Even more intriguing is that those resonances were recorded in inelastic co-tunnelling measurements in the weak-coupling regime[16]. Because in ref. 12 no comparative measurement for the weak-coupling regime was reported, the missing of resonances could not be unambigously interpreted as a signature of the Kondo effect. From a closer inspection of other experimental reports for the Kondo regime[5,7,10,17], we notice that the absence of some resonances seems systematic.

In the following, we study the low-temperature nonlinear electron transport in a very clean CNT quantum dot[18]. By simply sweeping a gate voltage[8,19], we could tune the same CNT device from a weak-coupling regime, where Coulomb diamonds and inelastic co-tunnelling are observed, to a Kondo regime with strong many-body correlations to the leads. Then, using nonlinear magnetospectroscopy, transport resonances have been measured. The two regimes have been described using accurate transport calculations based on perturbative and nonperturbative approaches in the coupling, respectively. The missing resonances in the Kondo regime have been clearly identified, and their suppression fully taken into account by the transport theory. Accounting for both spin and orbital degrees of freedom, we discuss a global $SU(2) \otimes SU(2)$ symmetry related to the presence of two Kramers pairs in realistic CNT devices with spin–orbit coupling (SOC)[20–23] and valley mixing[16,21,24–26]. In virtue of an effective exchange interaction, virtual transtions that flip the Kramers pseudospins yield low-energy many-body singlet states with net zero Kramers pseudospin. This result in turn reveals that the transport resonances suppressed in the deep Kondo regime are associated with virtual processes that do not flip the Kramers pseudospin.

Results

Measurement and modelling of transport regimes. The device under study consists of a semiconducting CNT, grown *in situ* on top of two platinum contacts, used as normal metal source and drain leads. Details of the device fabrication were reported previously[17] (see also the Methods). The CNT junction is suspended over an electrostatic gate and can be modelled as a single semiconducting quantum dot of size imposed by the contact separation ($\approx$200 nm). All the measurements were performed at a mixing chamber temperature of about $T_{exp} = 30$ mK, which sets a lower bound to the actual electronic temperature. The set-up includes the possibility to fully rotate an in-plane magnetic field up to 1.5 T.

The CNT-level spectrum is depicted in Fig. 1a,b. Transverse bands, represented by the coloured hyperbolae in Fig. 1a, emerge from the graphene Dirac cones as a consequence of the quantization of the transverse momentum $k_\perp$. Bound states (bullets) are because of the quantization of the longitudinal momentum $k_{||}$. Fourfold spin-valley degeneracy yields the exotic spin plus orbital $SU(4)$ Kondo effect[5,6,8,13,17,27,28]. The SOC removes the spin degeneracy of the transverse bands in the same valley (red and blue hyperbolae), and hence the $SU(4)$ symmetry[6,10,12,14,15,17,28,29]. Owing to the time-reversal symmetry, for each $k_{||}$ a quartet of states consisting of two Kramers pairs splitted by the energy $\Delta = \Delta_{SO}$ arises. When also valley mixing is present, with the energy scale $\Delta_{KK'}$, orbital states are formed that are superpositions of valley states. A quartet now consists of two Kramers doublets at energies $\varepsilon_d = \pm\Delta/2$, with $\Delta = \sqrt{\Delta_{SO}^2 + \Delta_{KK'}^2}$, see Fig. 1b.

By sweeping the gate voltage, the chemical potential is moved from above (electron sector) to below (hole sector) the charge neutrality point, and quadruplets of states are thus successively emptied. This pattern is visible in a typical measurement of the differential conductance dI/dV versus the bias voltage V_{sd} and the gate voltage V_g, Fig. 1c,d, which exhibits a characteristic fourfold periodicity. Figure 1c displays such a stability diagram for the electron sector, where Coulomb diamonds and inelastic co-tunnelling excitation lines are visible. Owing to significantly different ratios Γ/U of the tunnel coupling to the charging energy in the valence and conduction regimes, Kondo physics dominates for odd hole number in the hole sector shown in Fig. 1d.

In order to investigate the dominant transport mechanisms, we have performed transport calculations for both regimes, using a standard minimal model for a longitudinal mode of a CNT quantum dot with SOC and valley mixing terms[16,18]. The explicit form of the model Hamiltonian $\hat{H}_{CNT}$ and the parameters used for the transport calculations are provided in the Methods. The transport calculations in the electron regime implement a perturbation theory that retains all tunnelling contributions to the dynamics of the CNT-reduced density matrix up to second order in the tunnel coupling Γ. This approximation thus accounts for Coulomb blockade (first order in Γ) and leading-order co-tunnelling processes (second order in Γ), and it is expected to give accurate results for small ratios Γ/k_BT and Γ/U (ref. 30). The results of the calculations for the differential conductance are shown in Fig. 1g—a gate trace in Fig. 1e. The perturbative theory reproduces the position of the inelastic co-tunnelling thresholds (panels 1c and 1g). In the gate trace of Fig. 1e, the experimental peaks are wider than the theoretical ones. Because in the latter the broadening is solely given by the temperature, this indicates that higher-order terms are responsible for a broadening of the order Γ and for a Lamb shift of the experimental peaks[31–33]. In this work we are interested only in the evolution of the co-tunnelling resonances in magnetic field, which is well captured by the perturbative approach as long as Kondo ridges are not yet formed.

This situation radically changes in the hole sector where the gate trace reveals Kondo ridges for odd hole numbers. The theoretical trace in Fig. 1f is the outcome of a nonperturbative numerical density-matrix numerical renormalization group (DM-NRG) calculation[34] that uses the same model Hamiltonian but with slightly different parameters. The strong suppression of the conductance in the valley with even hole occupancy is an indication of the breaking of the $SU(4)$ symmetry in the presence of SOC and valley mixing to an $SU(2) \otimes SU(2)$ one[29,35]. In the DM-NRG calculations, the two-particles exchange J was not included because of high computational costs. The latter further reduces the symmetry in the 2h valley (see, for example, the spectrum in Fig. 2b), and hence the experimental conductance is more rapidly suppressed in that valley than as predicted by our simulations. On the other hand, J is not relevant for describing the spectrum in the 3h and 1h cases (Fig. 2a,c), which is the focus of the present work.

In the DM-NRG calculations, the fit to the experiment was performed assuming a temperature of $T = 30$ mK. From the so extracted parameters we evaluate the temperature dependence of the conductance at $-\varepsilon_d = U/2 - \Delta/2$, and $-\varepsilon_d = 5U/2 + \Delta/2$,

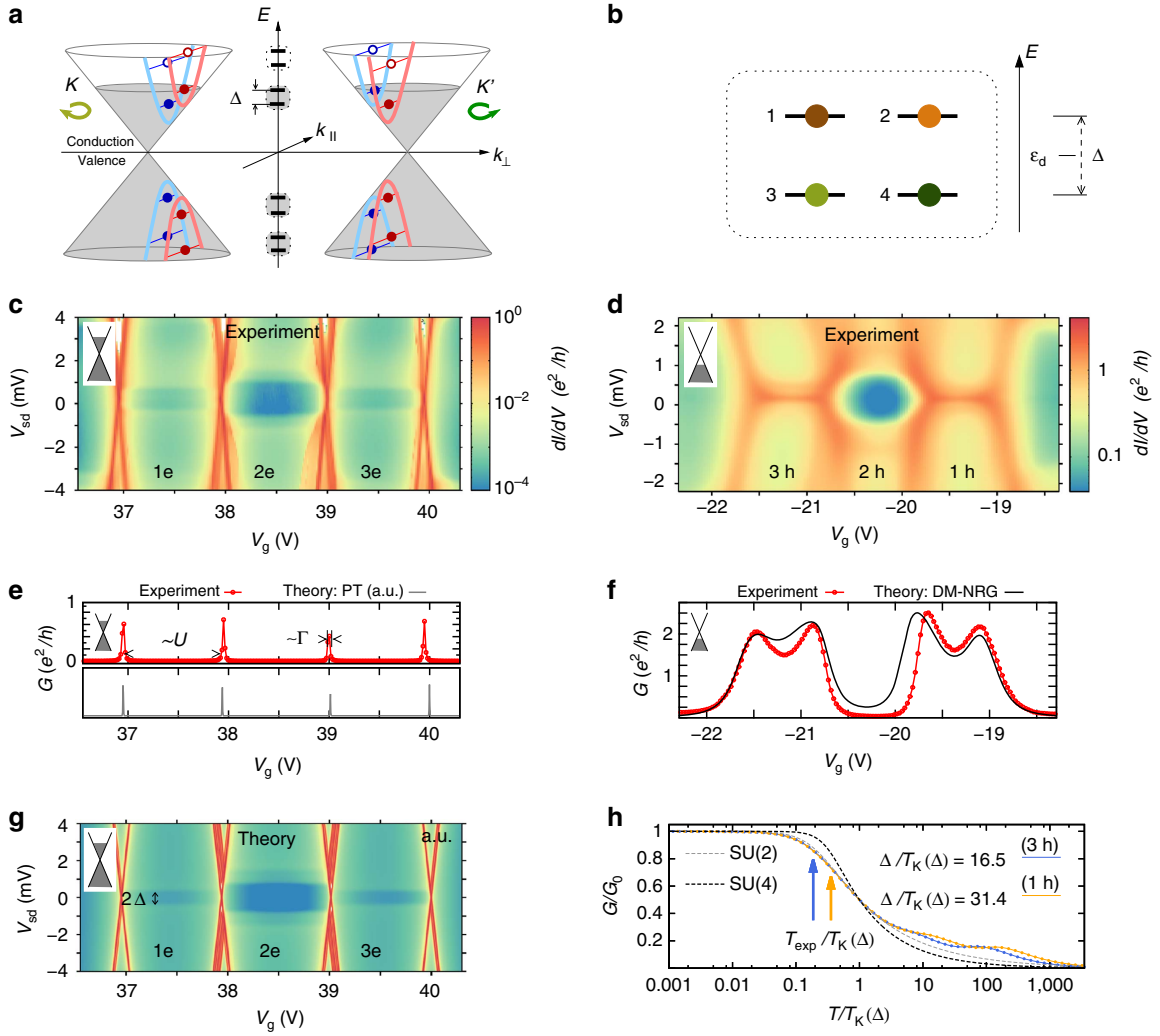

Figure 1 | Transport regimes and bound states of a CNT quantum dot. (**a**) A CNT with spin–orbit coupling is characterized by spin (blue, red) and valley (K, K′) resolved transverse modes (blue and red hyberbolae). The CNT chemical potential (upper limit of the shaded regions of the Dirac cones) is adjusted by sweeping the gate voltage from positive values (electron regime) to negative values (hole regime). Quantum confinement yields the quantization of the longitudinal momentum $k_{||}$ (empty/solid bullets denote empty/filled bound states). (**b**) A generic quadruplet of bound states is composed of two Kramers doublets separated by the inter-Kramers splitting Δ. (**c**,**d**) Experimental stability diagrams demonstrating the successive filling of a quadruplet with electrons (**c**), and holes (**d**). On the electron side, sequential transport is exponentially suppressed inside the Coulomb valleys; the dominant mechanism is co-tunnelling. The appearance of high conductance ridges at zero bias (**d**) in valleys with odd holes is a signature of the Kondo effect. (**e**,**f**) Experimental gate traces at zero bias are compared with theoretical predictions obtained with perturbative (**e**) and nonperturbative DM-NRG (**f**) approaches. (**g**) Theoretical stability diagram for the electron side reproducing the experiment of **c**. (**h**) Scaling behaviour of the linear conductance in the middle of the valleys with odd hole numbers, $G_0 \approx 2e^2/h$. The system lies in the crossover regime ($0.1 < T_{exp}/T_K(\Delta) < 1$), as pointed out by the arrows. T_K is the Kondo temperature determined from the DM-NRG calculation according to $G(T_K) = G_0/2$.

corresponding to gate voltage values located roughly in the middle of the 1h and 3h valleys, respectively, and extract the Kondo temperatures (see Fig. 1h). At such values of ε_d the Kondo temperature takes its minimal value in a given valley, which sets a lower bound for T_K (ref. 35). We find $T_K = 84$ mK and $T_K = 160$ mK for the 1h and 3h valleys, respectively. Correspondingly, $0.1 < T_{exp}/T_K < 1$, suggesting that the experiment is in the so-called Kondo crossover regime[1] also for the actual electronic and Kondo temperatures.

Virtual transitions revealed by magnetospectroscopy. Having set the relevant energy scales for both the electron and hole sectors, we proceed now with the investigation of magnetotransport measurements at finite source-drain bias, which have been performed for different fillings. A magnetic field **B** breaks time-reversal symmetry and thus the Kramers degeneracies. By performing inelastic co-tunnelling spectroscopy, we can get information on the lowest lying resonances of our interacting system. The magnetospectrum corresponding to electron filling $n_e = 1$, 2, 3 of a longitudinal quadruplet, as expected for the perturbative regime, is shown in Fig. 2a–c. For the case of odd occupancies, we call $\mathcal{T}$ transition processes within a Kramers pair; $\mathcal{C}$ and $\mathcal{P}$ operations are associated to inter-Kramers transitions, as shown in Fig. 2a,c. Panels 2d–2f and 2g–2i show magnetotransport measurements and theoretical predictions for the electron and hole regimes, respectively. In these panels the current second derivative d^2I/dV^2 is reported. We have preferred this quantity over the more conventional dI/dV (shown in the Supplementary Figs 4 and 5 and discussed in the Supplementary Note 4) to enhance eye visibility of the excitation spectra. In panels 2d–2f as well as 2h we have used our perturbative

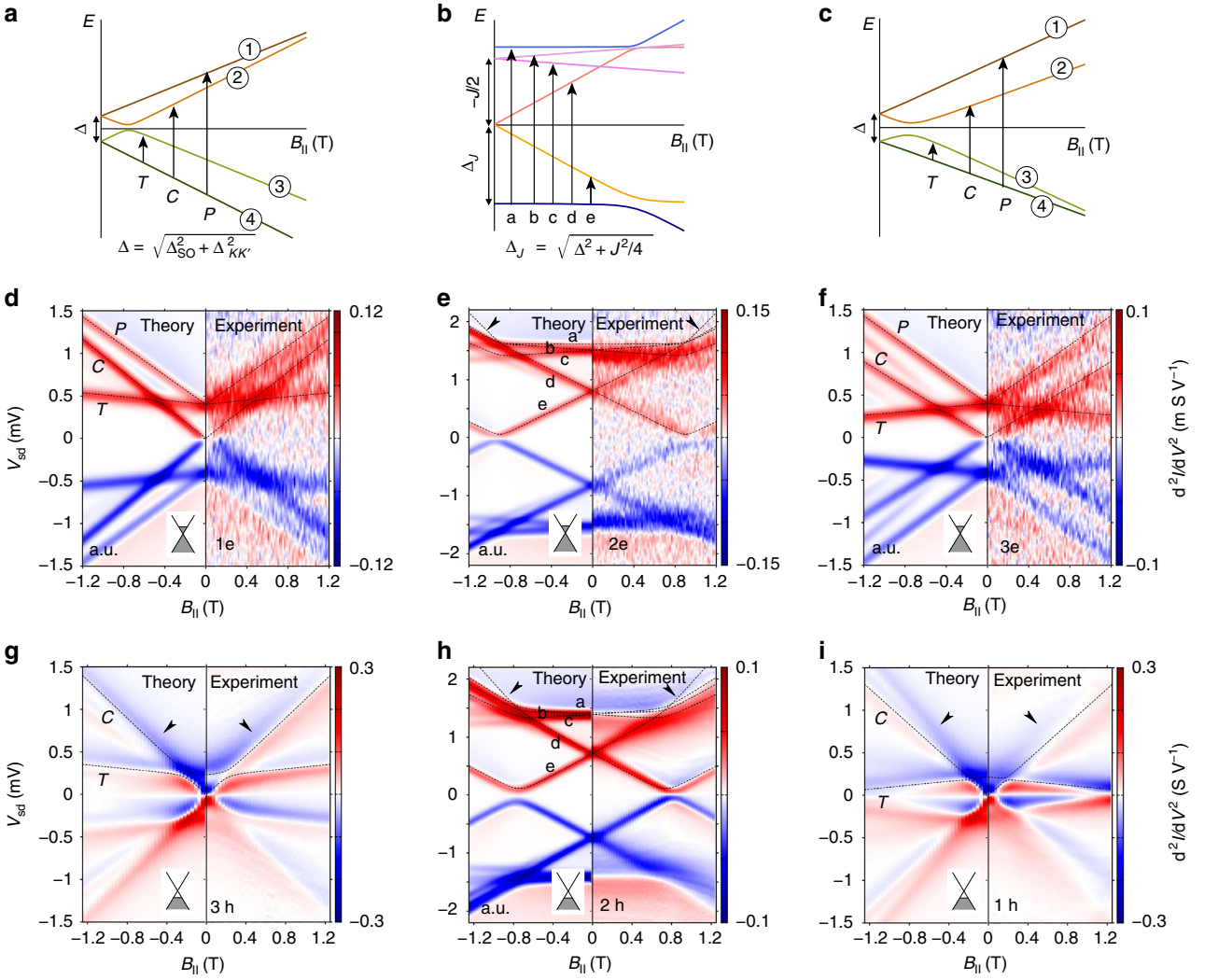

Figure 2 | Energy spectra and magnetotransport in both co-tunnelling and Kondo regimes. (**a**–**c**) Excitation spectra for electron filling ($n_e = 1, 2, 3$ from left to right). The parameters, Δ_{SO}, $\Delta_{KK'}$ and J account for SOC, valley mixing and exchange splitting, respectively. (**d**–**f**) Current second derivative d^2I/dV^2 in the electron regime at gate voltages fixed in the middle of the 1e, 2e and 3e charge states, as a function of bias voltage and parallel magnetic field. Each panel reports experimental data (positive magnetic field) and transport calculations (negative field). The dotted lines correspond to the transition energies from the ground state calculated directly from the spectra (**a**–**c**). At odd filling (**a**,**c**), all possible ground-state transitions, denoted by $\mathcal{C}$, $\mathcal{P}$ and $\mathcal{T}$, are observed in the experiment (**d**,**f**). Being signalled by co-tunnelling steps in the current first derivative, they yield maxima/minima in the second derivative. Likewise for even occupation, except for the 'a' transition at high field (marked by arrows), forbidden by selection rules. (**g**–**i**) d^2I/dV^2 maps in the hole regime for the 1h, 2h and 3h charge states. While the experimental results for the 2h and 2e cases are similar, the $\mathcal{P}$ transitions are no longer experimentally resolved, as predicted by the transport theory because of the Kondo effect (**g**,**i**). These missing resonances are indicated by arrows in **g**,**i**. In the Kondo regime $\mathcal{T}$ and $\mathcal{C}$ transitions yield maxima in the differential conductance, and hence zeroes in the second derivative. Near maxima (minima) of dI/dV the second derivative decreases (increases), that is, it changes from red to blue (blue to red) upon increasing the bias. The experimental part of **g**–**i** has been adapted from[17].

approach[30]. The calculations in Fig. 2g,i, in contrast, are based on the Keldysh effective action (KEA) method[36,37] and are nonperturbative. The nature of the dominant inelastic transitions is clearly identified by simply looking at the excitation spectrum (dashed lines in Fig. 2d–i). All inelastic transitions from the ground state are resolved in the co-tunnelling spectroscopy performed in the low coupling electron regime, similar to previous reports[16]. When inspecting the hole regime, it is clear that only for the 2h case, panel 2h, the experimental data can be interpreted by means of a simple co-tunnelling excitation spectrum; moreover, the 2e and 2h co-tunnelling spectra are very similar. In the 1h and 3h cases shown in panels 2g, 2i Kondo correlations dominate the low-energy transport, and differences with respect to the electron sector are seen. The zero-bias Kondo peak does not immediately split as the field is applied; rather the splitting occurs at a critical field such that the energy associated to the inelastic $\mathcal{T}$ transition is of the order of the Kondo temperature[1]. In the 1 h valley, the lowest pair of levels merges again for values of the field of $\sim$1.2 Tesla, yielding a Kondo revival[5,29]. Bias traces of the differential conductance highlighting the revival are shown in the Supplementary Fig. 3 and analysed in the Supplementry Note 3. Striking here is the observation that, in contrast to the 1e and 3e cases, only one of the two inter-Kramers transitions is resolved in the experimental data for the 3h and 1h valley. However, in particular for the 1h case, the $\mathcal{P}$ and $\mathcal{C}$ excitation lines, as expected from the excitation spectrum, should be separated enough to be experimentally distinguishable, similar to the 3e case. By comparing with the

excitation spectrum (dashed lines in panels 2g, 2i), we conclude that it is the $\mathcal{P}$ transition, which is not resolved. Our KEA transport theory qualitatively reproduces these experimental features.

Magnetotransport measurements performed for other quadruplets both in the conduction and valence regimes exhibit qualitatively similar features (see Supplementary Figs 6–8, Supplementary Table 1 and Supplementry Note 5), and hence confirm the robustness of the suppression of $\mathcal{P}$ transitions in the Kondo regime. Our results naturally reconcile the apparently contradictory observations in refs 12,16. Furthermore, they suggest that the inhibition of selected resonances in the Kondo regime is of fundamental nature.

Fundamental symmetries of correlated CNTs. To understand the experimental observations microscopically, we have analysed those symmetries of an isolated CNT, which also hold in the presence of on-site Coulomb repulsion typical of Anderson models.

In the absence of a magnetic field, one finds a $U(1) \otimes U(1) \otimes SU(2) \otimes SU(2)$ symmetry related to the existence of two pairs of time-reversal degenerate doublets (see Fig. 1b) called in the following upper (u) and lower (d) Kramers channels. The $U(1)$ symmetries reflect charge conservation in each Kramers pair with generators $\hat{Q}_\kappa=\frac{1}{2}\sum_{j\in\kappa}\left(\hat{n}_j-\frac{1}{2}\right)$, which measure the charge of the pair with respect to the half-filling. Here is $j=(1, 2)$ or $(3, 4)$ for $\kappa=u$ or d. The $SU(2)$ symmetries are generated by the spin-like operators $\hat{\mathbf{J}}_\kappa=\frac{1}{2}\sum_{j,j'\in\kappa}\hat{d}_j^\dagger\boldsymbol{\sigma}_{j,j'}\hat{d}_{j'}$. Here $\boldsymbol{\sigma}$ is the vector of Pauli matrices. Physically, $\hat{J}^z_{\rm u}=(\hat{n}_1-\hat{n}_2)/2$ and $\hat{J}^z_{\rm d}=(\hat{n}_4-\hat{n}_3)/2$ account for the charge unbalance within the Kramers pair. Thus, an isolated CNT with one electron or a hole only in the quadruplet has a net Kramers pseudospin (and charge). Figure 3a shows the two degenerate ground-state configurations $|\Downarrow;-\rangle$, $|\Uparrow\ -\rangle$ of the isolated CNT with an unpaired effective spin ($\Downarrow$ or $\Uparrow$) in the lowest Kramers pair and no occupation (symbol '$-$') of the upper Kramers pair. In the weak-coupling regime, a perturbative approach to linear transport accounts for elastic co-tunnelling processes involving the doubly degenerate ground-state pair[38]. These virtual transitions are denoted $\mathcal{I}$ or $\mathcal{T}$ when they involve the same state or its Kramers partner, respectively (see Fig. 3a). A finite magnetic field breaks the $SU(2)$ symmetries. However, former degenerate CNT states can still be characterized according to the eigenvalues of the $\hat{Q}_\kappa$ and $\hat{J}^z_\kappa$ operators, since they commute with the single-particle CNT Hamiltonian, which has in the Kramers basis the form (see Methods):

$$\hat{H}_0=\sum_{\kappa=\pm}\left(\bar{\varepsilon}(\mathbf{B})+\kappa\frac{\bar{\Delta}(\mathbf{B})}{2}\right)\hat{N}_\kappa+2\delta\varepsilon(\mathbf{B})+\kappa\delta\Delta(\mathbf{B})\hat{J}^z_\kappa, \quad (1)$$

where $u/d=+/-$, $\hat{N}_\kappa=2\hat{Q}_\kappa+1$, and at zero field is $\bar{\Delta}(B=0)=\Delta$, $\bar{\varepsilon}(B=0)=\varepsilon_{\rm d}$, $\delta\varepsilon=\delta\Delta=0$. Hence, our finite bias and finite magnetic field spectroscopy allows us to clearly identify the relevant elastic and inelastic virtual processes according to the involved Kramers charge and spin. As illustrated in Fig. 3b, in the weak tunnelling regime only energy differences matter in our model, and hence both intra-Kramers ($\mathcal{I}$, $\mathcal{T}$) and inter-Kramers ($\mathcal{P}$, $\mathcal{C}$) transitions are expected in transport. In the Kondo regime this picture changes. As we shall demonstrate, emerging Kondo correlations lead to the progressive screening of the Kramers pseudospin of the dot by the conduction electrons.

To this aim we observe that, when a sizeable tunnel coupling to the leads is included, the CNT charge and pseudospin operators $\hat{Q}_\kappa$ and $\hat{\mathbf{J}}_k$ are no longer symmetries of the coupled system, since the tunnelling does not conserve the dot particle number. The occurrence of the Kondo effect, however, suggests that the CNT quantum numbers $j=1, 2, 3, 4$ are carried also by the conduction electrons and conserved during tunnelling[13]. This is the case when the dot is only a segment of the CNT (see Supplementary Fig. 1). Following ref. 35, we hence introduce charge, $\hat{\mathcal{Q}}_\kappa=\hat{Q}_\kappa+\hat{Q}_{{\rm L},\kappa}$, and pseudospin, $\hat{\boldsymbol{\mathcal{J}}}_\kappa=\hat{\mathbf{J}}_\kappa+\hat{\mathbf{J}}_{{\rm L},\kappa}$, operators of the coupled CNT plus leads (L) system. Under the assumption that the tunnelling couplings are the same within each Kramers channel $\kappa=u,d$, the total Hamiltonian (see Supplementary Methods) commutes with the charge and pseudospin operators $\hat{\mathcal{Q}}_\kappa$ and $\hat{\boldsymbol{\mathcal{J}}}_\kappa$, which hence generate a $U(1) \otimes U(1) \otimes SU(2) \otimes SU(2)$ symmetry of the coupled system. As a consequence, many-body states can be characterized by the quadruplet of eigenvalues

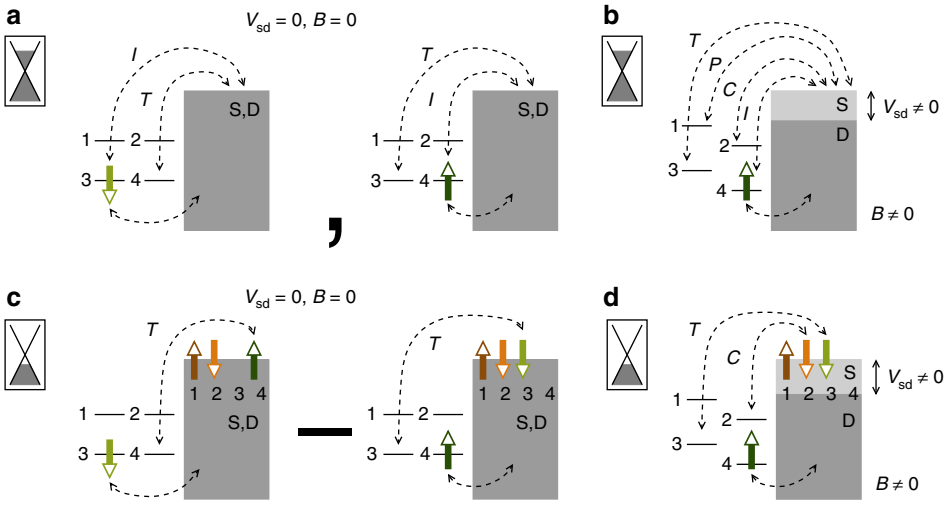

Figure 3 | Ground-state configurations and virtual processes of a CNT quantum dot with one-electron filling in the co-tunnelling and Kondo regimes. (**a**) In the co-tunnelling regime the one-electron ground state is doubly degenerate, with opposite values of the Kramers pseudospin. Elastic co-tunnelling processes to source (S) and drain (D) leads (grey areas) involving the same pseudospin, $\mathcal{I}$, and its Kramers partner, $\mathcal{T}$, contribute to the linear transport. (**b**) Kramers degeneracy is broken by a magnetic field. A finite bias allows us to identify the three inelastic processes $\mathcal{T}$, $\mathcal{P}$ and $\mathcal{C}$, which connect the bound states within a quadruplet. (**c**) The ground state in the Kondo regime is a singlet with no net Kramers pseudospin. Virtual $\mathcal{T}$ fluctuations which involve a pseudospin flip dominate at low energies. (**d**) At finite bias voltages the inelastic $\mathcal{T}$, $\mathcal{C}$ transitions, which involve a pseudospin flip, are the most relevant in the deep Kondo regime.

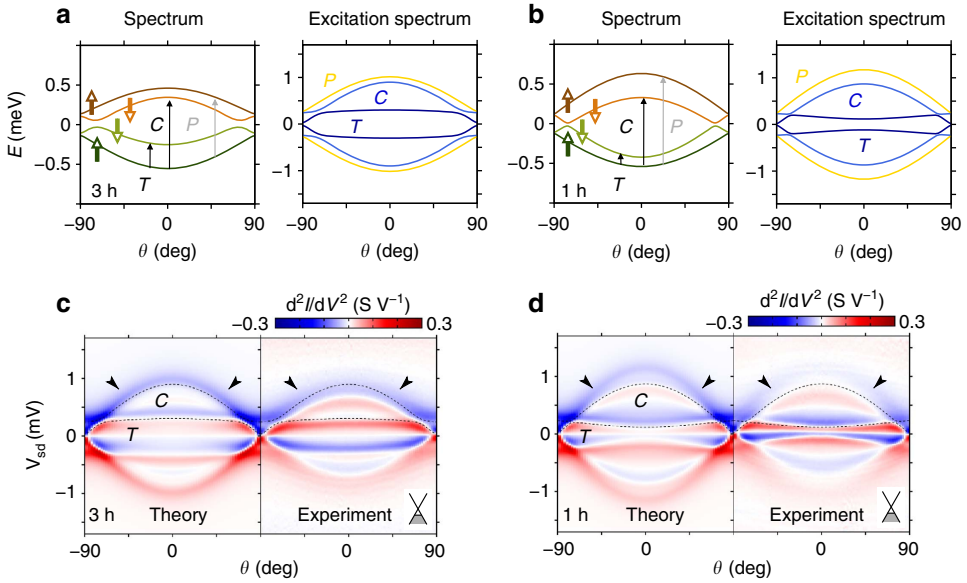

Figure 4 | Angular dependence of both spectrum and transport characteristics as the magnetic field is rotated in the CNT plane. (**a**,**b**) Sketch of the spectrum and excitation spectrum at 3h and 1h fillings, respectively, as a function of the polar angle θ formed by an applied magnetic field and the CNT axis. A classification of the inelastic transtions according to the $\mathcal{T}$, $\mathcal{C}$ and $\mathcal{P}$ operations is still possible. (**c**,**d**) As-measured and KEA transport calculations for the current's second derivative d^2I/dV^2. The absence of $\mathcal{P}$ transitions is independent of the direction of the applied field. The experimental part of **d** has been adapted from ref. 17. The magnetic field magnitude in **a**–**d** is set to 0.8 T.

$(\mathcal{Q}_d, \mathcal{Q}_u; \mathcal{J}_d, \mathcal{J}_u)$, where the highest eigenvalue $\mathcal{J}_\kappa$ of $\hat{\mathcal{J}}^z_\kappa$ is indicated in the quadruplet. This notation gives direct access to the eigenvalues $\mathcal{J}_\kappa(\mathcal{J}_\kappa+1)$ of $\hat{\boldsymbol{\mathcal{J}}}^2_\kappa$. Such quadruplets can be numerically calculated within our scheme for the Budapest DM-NRG code[39], and yield (for the valleys with one electron or one hole) a *singlet* ground state characterized by the quadruplet (0, 0; 0, 0). Thus, '0' is also eigenvalue of $\hat{\boldsymbol{\mathcal{J}}}^2_u$ and $\hat{\boldsymbol{\mathcal{J}}}^2_d$. That is, we find a unique ground state with no net pseudospin. This situation is illustrated in Fig. 3c: because of $\mathcal{Q}_k$=0, the Kramers channels are half-filled (two charges per channel), whereby one charge arises from the electron trapped in the CNT itself. For $\Delta=0$ this CNT charge is equally distributed among the two channels, while for large values of $\Delta/T_K(\Delta)$, as in our calculation (see Fig. 1h), it is mainly in the lowest Kramers channel. Thus, at zero temperature the localized CNT pseudospin is fully screened by an opposite net pseudospin in the leads. In the orthonormal basis $\{|m\rangle \otimes |n\rangle_L\}$, spanned by the pseudospin eigenstates of CNT and leads, this ground state is characterized by the entangled configuration $\frac{1}{\sqrt{2}}[|\Uparrow;\ -\rangle \otimes |\Downarrow;\ \Downarrow,\ \Uparrow\rangle_L - |\Downarrow;\ -\rangle \otimes |\Uparrow;\ \Downarrow,\ \Uparrow\rangle_L]$ of dot and leads pseudospins.

In the standard spin-1/2 Kondo effect, the appearance of a unique singlet ground state with no net spin is the result of the screening of the quantum impurity spin by the conduction electron spins because of the antiferromagnetic character of the coupling constant between such degrees of freedom[1]. Triplets are excited states of the system. To interpret the spin-1/2 Kondo effect in quantum dots, it is possible to derive from an Anderson model an effective Kondo Hamiltonian[40] given by the product of the quantum dot spin and the conduction electron spin. The coupling constant for this product is positive and thus antiferromagnetic. In addition, for the more complex case of a CNT, effective Kondo Hamiltonians have been derived, with positive coupling constants for Kramers channels identified by orbital and spin degrees of freedom[13,41]. The antiferromagnetic character of the coupling constants remains also when, as in our case, the more abstract Kramers pseudospin is used.

A natural consequence of the antiferromagnetic nature of the correlations is that at low temperatures and zero-bias elastic virtual transitions, which flip the pseudospin, that is, $\mathcal{T}$ transitions, are favoured, as depicted in Fig. 3c. Similarly, $\mathcal{C}$ transitions are inelastic processes that flip the pseudospin and become accessible at finite bias, as shown in Fig. 3d. They connect the singlet ground state to an excited state where the CNT charge is located in the upper Kramers channel. Our results suggest that $\mathcal{P}$ transitions are inhibited because they involve virtual transitions that conserve the pseudospin.

Entanglement of Kramers pseudospins. To further confirm that it is the Kramers pseudospins and not distinct spin or orbital degrees of freedom, which should be considered in the most general situations, we report results for the differential conductance as a function of the angle θ formed by the magnetic field and the CNT's axis. The combined action of SOC, valley mixing and non-collinear magnetic field mixes spin and valley degrees of freedom which, in general, are no longer good quantum numbers to classify CNT states. Nevertheless, the three discrete $\mathcal{T}$, $\mathcal{P}$ and $\mathcal{C}$ operations still enable us to identify the inelastic transitions in the 1h and 3h case, independent of the direction of the magnetic field. The angular dependence of both energy and excitation spectra for a fixed magnetic field amplitude is shown in Fig. 4a,b for the 3h and 1h fillings, respectively. The corresponding transport spectra are shown in Fig. 4c,d, respectively. A perpendicular magnetic field almost restores (for our parameter set) Kramers degeneracy, thus revitalizing the Kondo resonance for this angle. As the field is more and more aligned to the CNT's axis, the degeneracy is removed, which also enables us to distinguish between $\mathcal{P}$ and $\mathcal{C}$ transitions. As in the axial case of Fig. 2, only the inelastic resonance associated with the $\mathcal{C}$ transition is clearly resolved in both the experiment and theory.

Entropy and specific heat. Usually, quantum entanglement suffers from decoherence effects[42,43]. The Kondo–Kramers singlets, however, are associated with a global symmetry of the quantum dot-plus lead complex, and are robust against thermal fluctuations or finite bias effects as long as the impurity is in the

Table 1 | Parameter set.

	Holes (shell $N_h=6$)	Electrons (shell $N_e=6$)
Δ_{SO} (meV)	−0.21	−0.4
$\Delta_{KK'}$ (meV)	0.08	0.04
μ_{orb} (meV per T)	0.51 (3h), 0.51 (2h), 0.55 (1h)	0.43
U (meV) PT		26,5
U (meV) NRG	4,7	
U (meV) KEA	∞ (3h, 1h)	
J (meV) PT	−1.35	−1.4
$\Delta_\mu B_{\|\|}$ (meV per T)	−0.05	−0.06
$e\Delta V_{sd}$ (meV)	0.12	0.28

CNT, carbon nanotube; KEA, Keldysh effective action; NRG, numerical renormalization group; PT, perturbation theory.
The table shows the parameters used to fit the electronic transport spectra of the CNT in the gate voltage region shown in the main text. It corresponds to the valence quadruplet $N_h=6$ (hole transport), and the conduction quadruplet $N_e=6$ (electron transport), counting the Coulomb diamonds from the band gap. PT, NRG and KEA refer to the three theoretical methods used in our calculations (see text). The experimental data for each Coulomb valley are offset by ΔV_{sd}, and tilted in the magnetic field by $\Delta_\mu B_{||}$, resulting in an asymmetry between the measurement in fields parallel and antiparallel to the CNT axis. In all the plots presented in the work both the offset and the tilt have been removed.

Fermi liquid regime[1] ($T<0.01\ T_K$ for our experiment). For larger energy scales, $0.01<T/T_K<1$ the impurity is not fully screened, but Kondo correlations persist yielding universal behaviour of relevant observables, as seen, for example, in Fig. 1h at the level of the linear conductance. In order to further investigate the impact of thermal fluctuations on Kondo correlations, we have calculated the temperature dependence of the impurity entropy $S_{CNT}=S_{tot}-S_L$, where the S_i is thermodynamic entropy, and of the impurity-specific heat[44] (see Supplementry Note 1 and Supplementary Fig. 2). The conditional entropy $S_{CNT}(T)$ remains close to zero up to temperatures $T\approx 0.01\ T_K$, indicating that the system is to a good approximation in the singlet ground state. At higher temperatures, the impurity entropy grows, but universality is preserved up to temperatures close to T_K, at which the entropy approaches the value k_B log2.

Discussion

Our results show that specific low-energy inelastic processes, observed in the perturbative co-tunnelling regime, tend to be blocked in the Kondo regime because of antiferromagnetic-like correlations, which at zero temperature yield a many-body ground state with net zero Kramers pseudospin. This signature of the Kondo effect is universal in the sense that it does not depend on the degree of the SOC or valley mixing specific to a given CNT. As such, it is also expected for $SU(4)$-correlated CNTs, which explains the missing inelastic resonance in the seminal work[5]. Furthermore, we believe that such pseudospin-selective suppression should be detectable also in a variety of other tunable quantum dot systems with emergent $SU(4)$ and $SU(2)\otimes SU(2)$ Kondo effects[4,11,45–48].

Because the screening is progressively suppressed by increasing the temperature or the bias voltage, it should be possible to recover such inelastic transitions by continuosly tuning those parameters. Indeed, signatures of the re-emergence of the $\mathcal{P}$ transition are seen in the KEA calculations and experimental traces at fields ~ 0.9 T in the form of an emerging shoulder (see Supplementary Fig. 3). Experiments at larger magnetic fields, not accessible to our experiment, are required to record the evolution of this shoulder, and thus the suppression of (non-equilibrium) Kondo correlations by an applied bias voltage.

Methods

Experimental fabrication. Devices were fabricated from degenerately doped silicon $Si/SiO_2/Si_3N_4$ wafers with a 500 nm-thick thermally grown SiO_2 layer and 50 nm Si_3N_4 on top. Metal leads separated by 200 nm were first defined by electron-beam lithography and deposited using electron-gun evaporation. A thickness of 2 nm Cr followed by 50 nm Pt was used. A 200 nm-deep trench was created using both dry-etching and wet-etching. A second step of electron-beam lithography was used to design a 50 nm-thin metallic local gate at the bottom of the trench. Catalyst was then deposited locally on top of the metal leads. CNTs were then grown by the carbon vapor deposition (CVD) technique to produce as clean as possible devices. Only devices with room temperature resistances below 100 kΩ were selected for further studies at very low temperature. A scanning electron microscopy of a device similar to the one measured in this work is shown in the Supplementary Fig. 1.

Transport methods. For the transport calculations, three different approaches have been used: the DM-NRG method, a real-time diagrammatic perturbation theory for the dynamics of the reduced density and the analytical KEA approach. Further details are discussed in the Supplementry Note 2.

Model CNT Hamiltonian. In our calculations we have used the standard model Hamiltonian for the longitudinal mode of a CNT accounting for SOC, valley mixing, on-site and exchange Coulomb interactions and an external magnetic field[18]. Regarding both SOC and the valley mixing as perturbations breaking the $SU(4)$ symmetry of the single-particle CNT Hamiltonian, it has the general form

$$\hat{H}_{CNT}=\hat{H}_d+\hat{H}_{SO}+\hat{H}_{KK'}+\hat{H}_U+\hat{H}_J+\hat{H}_B, \tag{2}$$

where $\hat{H}_d+\hat{H}_U$ is the $SU(4)$ invariant component. In the basis set $\{K'\uparrow, K'\downarrow, K\uparrow, K\downarrow\}$ indexed by the valley and spin degrees of freedom $\tau=K', K=\pm$ and $\sigma=\uparrow, \downarrow=\pm$, respectively, it reads

$$\hat{H}_d+\hat{H}_U=\varepsilon_d\sum_{\tau,\sigma=\pm}\hat{d}^\dagger_{\tau,\sigma}\hat{d}_{\tau,\sigma}+\frac{U}{2}\sum_{(\tau,\sigma)\neq(\tau',\sigma')}\hat{n}_{\tau,\sigma}\hat{n}_{\tau',\sigma'}, \tag{3}$$

with ε_d being the energy of the quantized longitudinal mode, which can be tuned through the applied gate voltage and U accounting for charging effects. Valley mixing and SOC break the $SU(4)$ symmetry with characteristic energies $\Delta_{KK'}$ and Δ_{SO}, respectively. The corresponding contributions read:

$$\hat{H}_{KK'}+\hat{H}_{SO}=\frac{\Delta_{KK'}}{2}\sum_{\tau,\sigma=\pm}\hat{d}^\dagger_{\tau,\sigma}\hat{d}_{-\tau,\sigma}+\frac{\Delta_{SO}}{2}\sum_{\tau,\sigma=\pm}\sigma\tau\hat{n}_{\tau,\sigma}. \tag{4}$$

The SOC term is a result of the atomic spin–orbit interaction in carbon, and thus exists also for ideally infinitely long CNTs[20]. The valley mixing, in contrast, is absent in long and defect-free CNTs. It only arises because of scattering off the boundaries in finite-length CNTs or because of disorder[21,25,26]. It is expected to be zero in disorder-free CNTs of the zig-zag class, because of angular momentum conservation rules, and finite in CNTs of the armchair class[26]. In our experiments, according to Table 1, the valley mixing is very small, which suggests a tube of the zig-zag class.

Similar to the SOC and valley mixing, the exchange interaction preserves time-reversal symmetry. Its microscopic form is not known for abritrary chiral angles. It has been evaluated so far for the case of pure armchair tubes[49], and for the zig-zag class[18,50] CNTs. Because the experiments suggest that our tube is of the zig-zag class, we choose in the following a form suitable to describe this case. It reads

$$\hat{H}_J=-\frac{J}{2}\sum_{\sigma=\pm}\left\{\hat{n}_{K,\sigma}\hat{n}_{K',\sigma}+\hat{d}^\dagger_{K,\sigma}\hat{d}^\dagger_{K',-\sigma}\hat{d}_{K,-\sigma}\hat{d}_{K',\sigma}\right\}, \tag{5}$$

with $J<0$ the exchange coupling. Finally, contributions arising from a magnetic field $\mathbf{B}$ contain both Zeeman and orbital parts. Decomposing $\mathbf{B}$ into components parallel and perpendicular to the tube axis, $B_{||}=B\cos\theta$ and $B_\perp=B\sin\theta$, respectively, one finds:

$$\begin{aligned}\hat{H}_B &= \hat{H}^Z_B+\hat{H}^{orb}_B\\ &= B_{||}\sum_{\tau,\sigma=\pm}\left(\tfrac{g}{2}\mu_B\sigma+\mu_{orb}\tau\right)\hat{d}^\dagger_{\tau,\sigma}\hat{d}_{\tau,\sigma}\\ &+ \tfrac{g}{2}\mu_B B_\perp\sum_{\tau,\sigma=\pm}\hat{d}^\dagger_{\tau,\sigma}\hat{d}_{\tau,-\sigma}.\end{aligned} \tag{6}$$

Notice that the spin and valley remain good quantum numbers in the presence of an axial field ($\theta=0,\pi$), while a perpendicular component flips the spin degrees of freedom. The parameters of the CNT Hamiltonian used to fit the experimental data shown in Figs 1, 2 and 4 are listed in Table 1.

Kramers charge and pseudospin representation. We call Kramers basis the quadruplet $\{|i\rangle\}$, $i=1, 2, 3, 4$ (shown in Fig. 1b), which diagonalizes the single-particle part $\hat{H}_0=\hat{H}_d+\hat{H}_{KK'}+\hat{H}_{SO}+\hat{H}_B$ of the CNT Hamiltonian. For magnetic fields parallel or perpendicular to the CNT axis, this Hamiltonian is easily diagonalized, see, for example, ref. 12. For other orientations of the field, because of the combined action of SOC and valley mixing, such states are a linear superposition of all the basis states $\{|\tau,\sigma\rangle\}$, such that neither the spin nor the valley are in general good quantum numbers any more. One has to resort to

numerical tools to find both the eigenvectors $\{|i\rangle\}$ and the eigenvalues ε_i, $i=1, 2, 3, 4$. The angular dependence of these eigenenergies is sketched in Fig. 4.

Despite the complexity inherent in the Hamiltonian $\hat{H}_0$, a closer inspection reveals the existence of conjugation relations among the quadruplet of states $i=1, 2, 3, 4$ generated by the time-reversal operator $\hat{\mathcal{T}}$, as well as by the particle–hole-like and chirality operators $\hat{\mathcal{P}}$ and $\hat{\mathcal{C}}=\hat{\mathcal{P}}\hat{\mathcal{T}}^{-1}$, respectively[12]. Specifically, the states are ordered such that (1, 2) and (3, 4) are time-reversal partners, while (1, 4) and (2, 3) are particle–hole partners. In the $\{|\tau,\sigma\rangle\}$ basis the operators read

$$\hat{\mathcal{T}} = -\hat{\kappa}\sum_{\tau,\sigma}\sigma\hat{d}^{\dagger}_{-\tau,-\sigma}\hat{d}_{\tau,\sigma}, \tag{7}$$

$$\hat{\mathcal{P}} = \hat{\kappa}\sum_{\tau,\sigma}\sigma\tau\hat{d}^{\dagger}_{-\tau,\sigma}\hat{d}_{\tau,\sigma}, \tag{8}$$

$$\hat{\mathcal{C}} = \sum_{\tau,\sigma}\tau\hat{d}^{\dagger}_{\tau,-\sigma}\hat{d}_{\tau,\sigma}, \tag{9}$$

where $\hat{\kappa}$ stands for the complex conjugation operator. In the absence of a magnetic field $\hat{\mathcal{T}}$ commutes with the total CNT Hamiltonian, yielding a single-particle spectrum with two degenerate Kramers doublets (1, 2) and (3, 4) separated by the inter-Kramers splitting $\Delta=\sqrt{\Delta_{\rm SO}^2+\Delta_{\rm KK'}^2}$ (see Fig. 1b). As far as the $\hat{\mathcal{P}}$ and $\hat{\mathcal{C}}$ operators are concerned, at zero magnetic field they are symmetries only in the absence of SOC and valley mixing. Since both anticommute with $\hat{H}_{\rm SO}+\hat{H}_{\rm KK'}$, it holds for $\mathcal{P}$-conjugated pairs, $\varepsilon_{1,2}(\Delta)=\varepsilon_{4,3}(-\Delta)$. A magnetic field breaks the time-reversal symmetry; however, because $\hat{H}_{\rm B}$ anticommutes with $\hat{\mathcal{T}}$, formerly degenerate Kramers states are still related to each other by Kramers conjugation. For an arbitrary magnetic field $\mathbf{B}$ time-reversal conjugation and particle–hole conjugation imply[12]:

$$\varepsilon_{1,4}(\mathbf{B}) = \varepsilon(\mathbf{B}) \pm \frac{1}{2}\Delta(\mathbf{B}), \tag{10}$$

$$\varepsilon_{2,3}(-\mathbf{B}) = \varepsilon_{1,4}(\mathbf{B}), \tag{11}$$

where $\varepsilon(\mathbf{B})$ and $\Delta(\mathbf{B})$ reduce to the longitudinal energy and Kramers splitting $\varepsilon_{\rm d}$ and Δ, respectively, at zero field.

These relations clearly suggest the introduction of auxiliary charge $\hat{N}_{ij}:=\hat{n}_i+\hat{n}_j$ and pseudospin $\hat{J}^z_{ij}=(\hat{n}_i-\hat{n}_j)/2$ operators, in terms of which we can write

$$\hat{H}_0 = \varepsilon(\mathbf{B})\hat{N}_{14}+\Delta(\mathbf{B})\hat{J}^z_{14}+\varepsilon(-\mathbf{B})\hat{N}_{23}+\Delta(-\mathbf{B})\hat{J}^z_{23}.$$

Introducing the average quantities $\bar{\Delta}(\mathbf{B}):=(\Delta(\mathbf{B})+\Delta(-\mathbf{B}))/2$, $\bar{\varepsilon}(\mathbf{B}):=(\varepsilon(\mathbf{B})+\varepsilon(-\mathbf{B}))/2$, as well as the differences $\delta\Delta(\mathbf{B}):=(\Delta(\mathbf{B})-\Delta(-\mathbf{B}))/2$, $\delta\varepsilon(\mathbf{B}):=(\varepsilon(\mathbf{B})-\varepsilon(-\mathbf{B}))/2$, the CNT Hamiltonian can be easily recast in terms of total charge and pseudospin of a Kramers pair. It reads:

$$\begin{aligned}\hat{H}_0 &= \left(\bar{\varepsilon}(\mathbf{B})+\tfrac{\bar{\Delta}(\mathbf{B})}{2}\right)\hat{N}_{12}+[2\delta\varepsilon(\mathbf{B})+\delta\Delta(\mathbf{B})]\hat{J}^z_{12}\\ &+ \left(\bar{\varepsilon}(\mathbf{B})-\tfrac{\bar{\Delta}(\mathbf{B})}{2}\right)\hat{N}_{43}+[2\delta\varepsilon(\mathbf{B})-\delta\Delta(\mathbf{B})]\hat{J}^z_{43}.\end{aligned}$$

Such equation is equation (1) in the main part of the manuscript upon calling $\hat{J}^z_{43}=\hat{J}^z_{\rm d}$, $\hat{J}^z_{12}=\hat{J}^z_{\rm u}$, and similarly $\hat{N}_{43}=\hat{N}_{\rm d}$, $\hat{N}_{12}=\hat{N}_{\rm u}$.

Data availability. The data that support the main findings of this study are available from the corresponding author upon request.

References

1. Hewson, A. C. *The Kondo Problem to Heavy Fermions* (Cambridge University Press, 1997).
2. Goldhaber-Gordon, D. *et al.* Kondo effect in a single-electron transistor. *Nature* **391,** 156–159 (1998).
3. Nygård, J., Cobden, H. C. & Lindelof, P. E. Kondo physics in carbon nanotubes. *Nature* **408,** 342–346 (2000).
4. Sasaki, S., Amaha, S., Asakawa, N., Eto, M. & Tarucha, S. Enhanced Kondo effect via tuned orbital degeneracy in a spin 1/2 artificial atom. *Phys. Rev. Lett.* **93,** 017205 (2004).
5. Jarillo-Herrero, P. *et al.* Orbital Kondo effect in carbon nanotubes. *Nature* **434,** 484–488 (2005).
6. Jarillo-Herrero, P. *et al.* Electronic transport spectroscopy of carbon nanotubes in a magnetic field. *Phys. Rev. Lett.* **94,** 156802 (2005).
7. Quay, C. *et al.* Magnetic field dependence of the spin-1/2 and spin-1 Kondo effects in a quantum dot. *Phys. Rev. B* **76,** 245311 (2007).
8. Makarovski, A., Zhukov, A., Liu, J. & Finkelstein, G. SU(2) and SU(4) Kondo effects in carbon nanotube quantum dots. *Phys. Rev. B* **75,** 241407 (2007).
9. Grap, E., Andergassen, S., Paaske, J. & Meden, V. Spin-orbit interaction and asymmetry effects on Kondo ridges at finite magnetic fields. *Phys. Rev. B* **83,** 115115 (2011).
10. Lan, Y.-W. *et al.* Interplay of spinorbit coupling and Zeeman effect probed by Kondo resonance in a carbon nanotube quantum dot. *Carbon. N. Y.* **50,** 3748–3752 (2012).
11. Tettamanzi, G. *et al.* Magnetic-field probing of an SU(4) Kondo resonance in a single-atom transistor. *Phys. Rev. Lett.* **108,** 046803 (2012).
12. Schmid, D. *et al.* Broken SU(4) symmetry in a Kondo-correlated quantum dot. *Phys. Rev. B* **91,** 155435 (2015).
13. Choi, M.-S., López, R. & Aguado, R. SU(4) Kondo effect in carbon nanotubes. *Phys. Rev. Lett.* **95,** 067204 (2005).
14. Fang, T.-F., Zuo, W. & Luo, H.-G. Kondo effect in carbon nanotube quantum dots with spin-orbit coupling. *Phys. Rev. Lett.* **101,** 246805 (2008).
15. Fang, T.-F., Zuo, W. & Luo, H.-G. Erratum: Kondo effect in carbon nanotube quantum dots with spin-orbit coupling. *Phys. Rev. Lett.* **104,** 169902 (2010).
16. Jespersen, T. S. *et al.* Gate-dependent spin-orbit coupling in multielectron carbon nanotubes. *Nat. Phys.* **7,** 348–353 (2011).
17. Cleuziou, J. P., N'Guyen, N. V., Florens, S. & Wernsdorfer, W. Interplay of the Kondo effect and strong spin-orbit coupling in multihole ultraclean carbon nanotubes. *Phys. Rev. Lett.* **111,** 136803 (2013).
18. Laird, E. A. *et al.* Quantum transport in carbon nanotubes. *Rev. Mod. Phys.* **87,** 703–764 (2015).
19. Cao, J., Wang, Q. & Dai, H. Electron transport in very clean, as-grown suspended carbon nanotubes. *Nat. Mater.* **4,** 745–749 (2005).
20. Ando, T. Spin-orbit interaction in carbon nanotubes. *J. Phys. Soc. Jpn.* **69,** 1757–1763 (2000).
21. Kuemmeth, F., Ilani, S., Ralph, D. C. & McEuen, P. L. Coupling of spin and orbital motion of electrons in carbon nanotubes. *Nature* **452,** 448–452 (2008).
22. Del Valle, M., Marganska, M. & Grifoni, M. Signatures of spin-orbit interaction in transport properties of finite carbon nanotubes in a parallel magnetic field. *Phys. Rev. B* **84,** 165427 (2011).
23. Steele, G. A. *et al.* Large spin-orbit coupling in carbon nanotubes. *Nat. Commun.* **4,** 1573 (2013).
24. Grove-Rasmussen, K. *et al.* Magnetic-field dependence of tunnel couplings in carbon nanotube quantum dots. *Phys. Rev. Lett.* **108,** 176802 (2012).
25. Izumida, W., Okuyama, R. & Saito, R. Valley coupling in fnite-length metallic single-wall carbon nanotubes. *Phys. Rev. B* **91,** 235442 (2015).
26. Marganska, M., Chudzinski, P. & Grifoni, M. The two classes of low-energy spectra in finite carbon nanotubes. *Phys. Rev. B* **92,** 075433 (2015).
27. Anders, F., Logan, D., Galpin, M. & Finkelstein, G. Zero-bias conductance in carbon nanotube quantum dots. *Phys. Rev. Lett.* **100,** 086809 (2008).
28. Ferrier, M. *et al.* Universality of non-equilibrium fluctuations in strongly correlated quantum liquids. *Nat. Phys.* **12,** 230–235 (2015).
29. Galpin, M. R., Jayatilaka, F. W., Logan, D. E. & Anders, F. B. Interplay between Kondo physics and spin-orbit coupling in carbon nanotube quantum dots. *Phys. Rev. B* **81,** 075437 (2010).
30. Koller, S., Leinsje, M., Wegewijs, M. & Grifoni, M. Density operator approaches to transport through interacting quantum dots: Simplifications in fourth-order perturbation theory. *Phys. Rev. B* **82,** 235307 (2010).
31. König, J., Schmid, J., Schoeller, H. & Schön, G. Transport through an Anderson quantum dot in the intermediate coupling regime. *Phys. Rev. B* **54,** 16820 (1996).
32. Pedersen, J. N. & Wacker, A. Tunneling through nanosystems: combining broadening with many-particle states. *Phys. Rev. B* **72,** 195330 (2005).
33. Dirnaichner, A. *et al.* Transport across a carbon nanotube quantum dot contacted with ferromagnetic leads: experiment and nonperturbative modeling. *Phys. Rev. B* **91,** 195402 (2015).
34. Bulla, R., Costi, T. A. & Pruschke, T. SU(4) Fermi liquid state and spin filtering in a double quantum dot system. *Rev. Mod. Phys.* **80,** 395–450 (2008).
35. Mantelli, D., Moca, C., Zaránd, G. & Grifoni, M. Kondo effect in a carbon nanotube with spin-orbit interaction and valley mixing: a DM-NRG study. *Phys. E* **77,** 180–190 (2016).
36. Smirnov, S. & Grifoni, M. Keldysh effective action theory for universal physics in spin-1/2 Kondo dots. *Phys. Rev. B* **87,** 121302 (2013).
37. Smirnov, S. & Grifoni, M. Nonequilibrium Kondo transport through a quantum dot in a magnetic field. *New J. Phys.* **15,** 073047 (2013).
38. Grabert, H. & Devoret, M. (eds). *Single Charge Tunneling* (Plenum Press, 1992).
39. Toth, A., Moca, C., Legeza, Ö. & Zaránd, G. Density matrix numerical renormalization group for non-Abelian symmetries. *Phys. Rev. B* **78,** 245109 (2008).
40. Schrieffer, J. & Wolff, P. Relation between the Anderson and Kondo Hamiltonians. *Phys. Rev.* **149,** 491–492 (1966).
41. Lim, J. S., Choi, M.-S., Choi, M. Y., López, R. & Aguado, R. Kondo effects in carbon nanotubes: from SU(4) to SU(2) symmetry. *Phys. Rev. B* **74,** 205119 (2006).
42. Buchleitner, A., Viviescas, C. & Tiersch, M. (eds). *Entanglement and Decoherence* (Springer, 2009).
43. Akulin, V. M., Sarfati, A., Kurizki, G. & Pellegrin, S. (eds). *Decoherence, Entanglement and Information Protection in Complex Quantum Systems* (Nato Science Series II, 2005).
44. Merker, L. & Costi, T. Numerical renormalization group calculations of impurity internal energy and specific heat of quantum impurity models. *Phys. Rev. B* **86,** 075150 (2012).

45. Borda, L. *et al.* SU(4) Fermi liquid state and spin filtering in a double quantum dot system. *Phys. Rev. Lett.* **90,** 026602 (2003).
46. Minamitami, E. *et al.* Symmetry-driven novel Kondo effect in a molecule. *Phys. Rev. Lett.* **109,** 086602 (2012).
47. Keller, A. *et al.* Emergent SU(4) Kondo physics in a spin-charge entangled quantum dot. *Nat. Phys.* **10,** 145–150 (2013).
48. Crippa, A. *et al.* Valley blockade and multielectron spin-valley Kondo effect in silicon. *Phys. Rev. B* **92,** 035424 (2015).
49. Mayrhofer, L. & Grifoni, M. The spectrum of interacting carbon nanotubes: exchange effects and universality. *Eur. Phys. J. B* **63,** 43 (2008).
50. Secchi, A. & Rontani, M. Coulomb versus spin-orbit interaction in few-electron carbon-nanotube quantum dots. *Phys. Rev. B* **80,** 041404 (R) (2009).

Acknowledgements

We acknowledge fruitful discussions with C. Strunk, A. Hüttel, G. Zaránd and C. P. Moca as well as the financial support by the Deutsche Forschungsgemeinschaft via SFB 689 and GRK 1570, and by the ERC Advanced Grant MolNanoSpin No. 226558.

Author contributions

M.N. performed the perturbative non-equilibrium calculations, S.S. evaluted the differential conductance in the Kondo regime using the non-equilibrium KEA approach, while D.M. did the equilibrium DM-NRG simulations. M.M. evaluated the magnetospectrum of the isolated nanotube and devised all the figures. N.-V.N. helped to fabricate and characterize the devices, J.-P.C. carried out and analysed the experiments, while W.W. supervised them. M.G. performed the theoretical analysis and wrote the manuscript with critical comments provided by all authors.

Additional information

Supplementary Information accompanies this paper at http://www.nature.com/naturecommunications

Competing financial interests: The authors declare no competing financial interests.

Reprints and permission information is available online at http://npg.nature.com/reprintsandpermissions/

How to cite this article: Niklas, M. *et al.* Blocking transport resonances via Kondo many-body entanglement in quantum dots. *Nat. Commun.* 7:12442 doi: 10.1038/ncomms12442 (2016).

Supplementary Figures

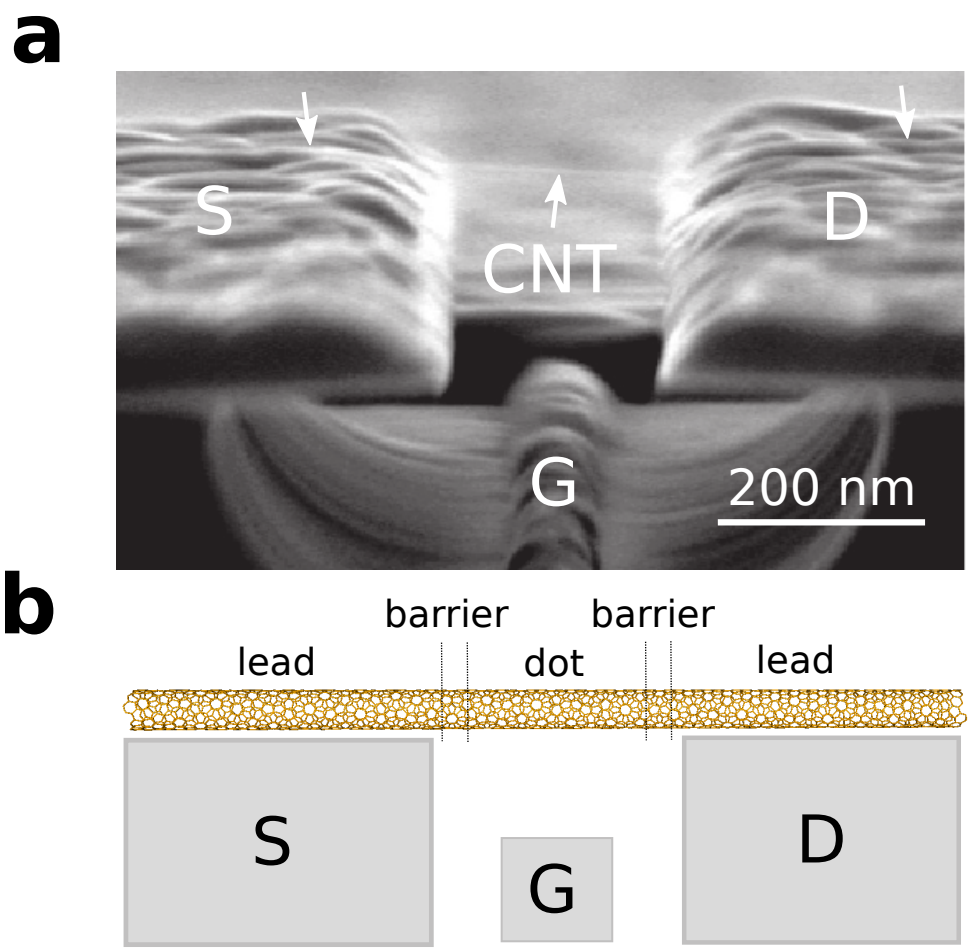

Supplementary Figure 1: Experimental device and schematics. **a,** Scanning electron microscopy of an ultraclean carbon nanotube based device similar to the one used in the experiment. A carbon nanotube (CNT) is suspended on top of litographically fabricated contacts. **b,** Schematic of the suspended CNT device. A segment of the CNT acts as a quantum dot separated by tunneling barriers from the rest of the tube. These latter parts of the nanotube act as electronic reservoirs from which charge carriers can tunnel into and out of the dot. The separation between the contacts defines the size of the quantum dot while the local back gate voltage influences the electrostatic profile seen by the charge carriers.

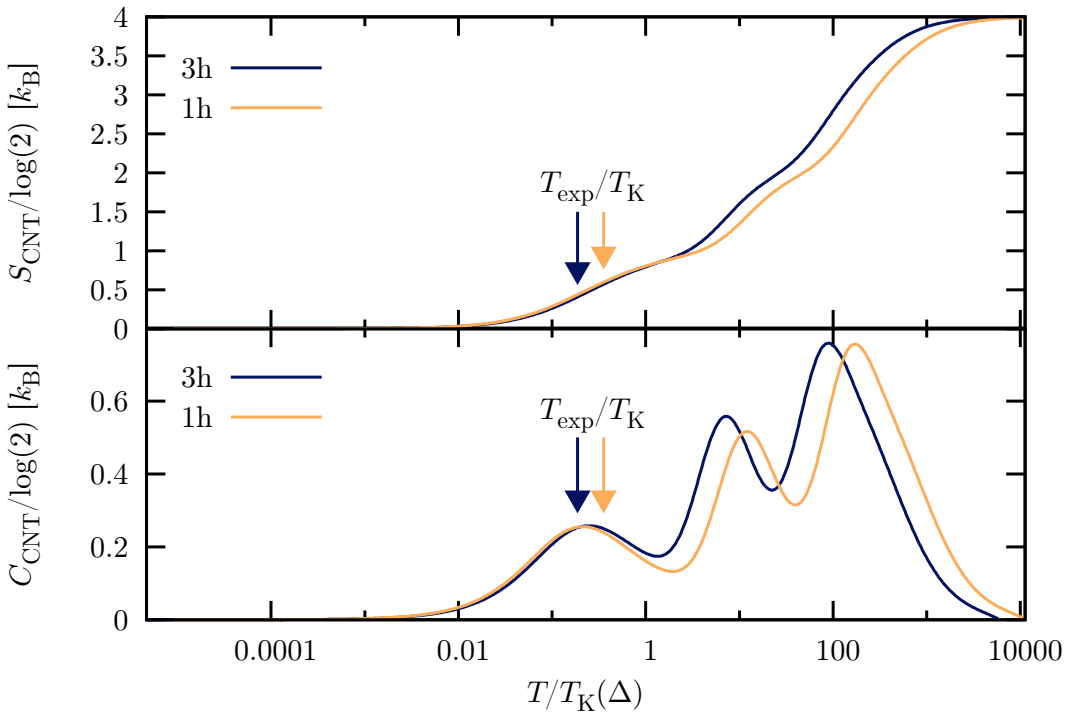

Supplementary Figure 2: Entropy and specific heat. Evolution of the impurity entropy and specific heat as a function of the temperature. The entropy is zero at zero temperature, indicating a non degenerate ground state. At finite temperatures, it remains close to zero up to temperatures of the order of 10^{-2} T_{K}, indicating that the system is to a good approximation in the ground state. At higher temperatures thermal fluctuations become more important but universality is preserved up to temperatures of the order of T_{K}, where a shoulder is observed. For even larger temperatures the upper Kramers charge state becomes accessible, yielding a shoulder in the vicinity of Δ; finally, a plateau with value $4k_{\mathrm{B}}\log 2$ is observed at about $U/2$. In the correspondence of such shoulders and of the plateau the specific heat has local minima.

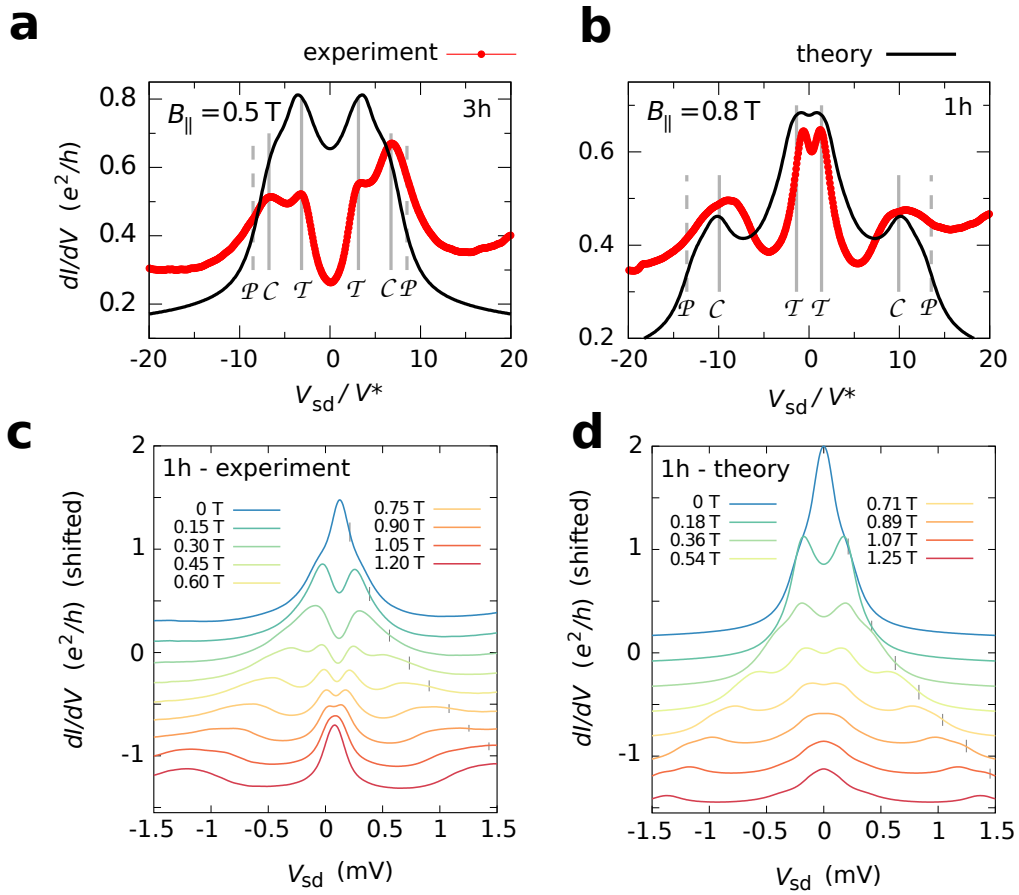

Supplementary Figure 3: Differential conductance at several magnetic field amplitudes. Bias traces of the differential conductance at various magnitudes of an applied axial magnetic field in the valence shell $N_h = 6$. **a** and **b,** Traces for the 3h and 1h valleys, respectively. The bias voltage is scaled by the voltage V^* at which the differential conductance at zero applied field reaches 0.8 of the conductance at zero bias. The vertical lines denote the position of the $\mathcal{P}$ and $\mathcal{C}$ resonances as expected from the addition spectrum. **c** and **d,** Experimental and theoretical bias traces for different values of the magnetic field. The qualitative evolution of the bias traces is similar in the theory and experiment, despite the shapes differ. The short vertical lines denoted the expected position of the $\mathcal{P}$ resonance, which is not visible at low fields, neither in the theoretical nor in the experimental traces. However, a signature of such resonance is observed at fields of about 0.9 T, indicating that Kondo screening has been weakened by the bias voltage necessary to induce a $\mathcal{P}$ transition.

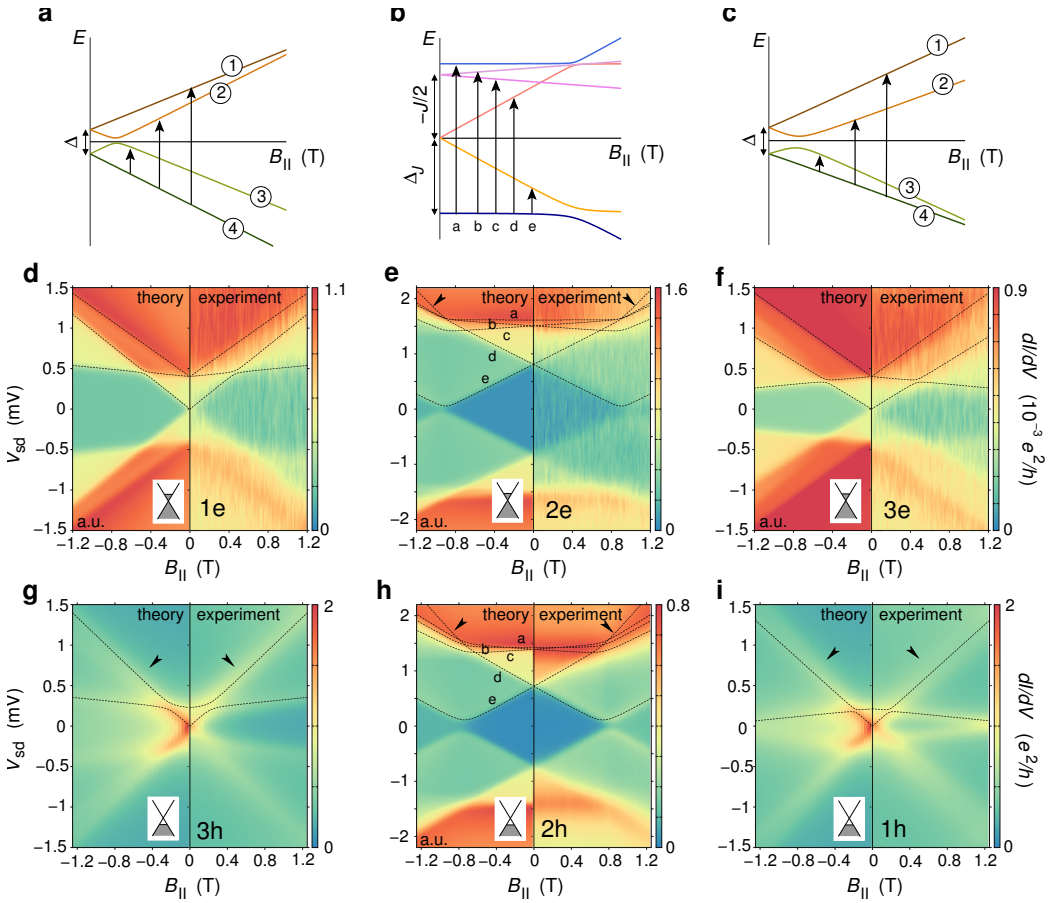

Supplementary Figure 4: Energy spectrum and differential conductance in parallel magnetic field. **a-c**, Excitation spectra for a longitudinal mode with electron filling (from left to right) $n_e = 1$ (1 electron, 3 holes), $n_e = 2$ (2 electrons, 2 holes) and $n_e = 3$ (3 electrons, 1 hole). **d-f**, dI/dV in the electron regime for gate voltages in the middle of the 1e, 2e and 3e charge states of the shell N_e. Each panel reports experimental data (positive magnetic field) and transport calculations (negative field). The dotted lines correspond to the transition energies from the ground state calculated directly from the spectra a)- c). The missing resonances are indicated by arrows. **g-i**, Panels analogous to the ones in d)-f), related to the N_h shell in the hole regime.

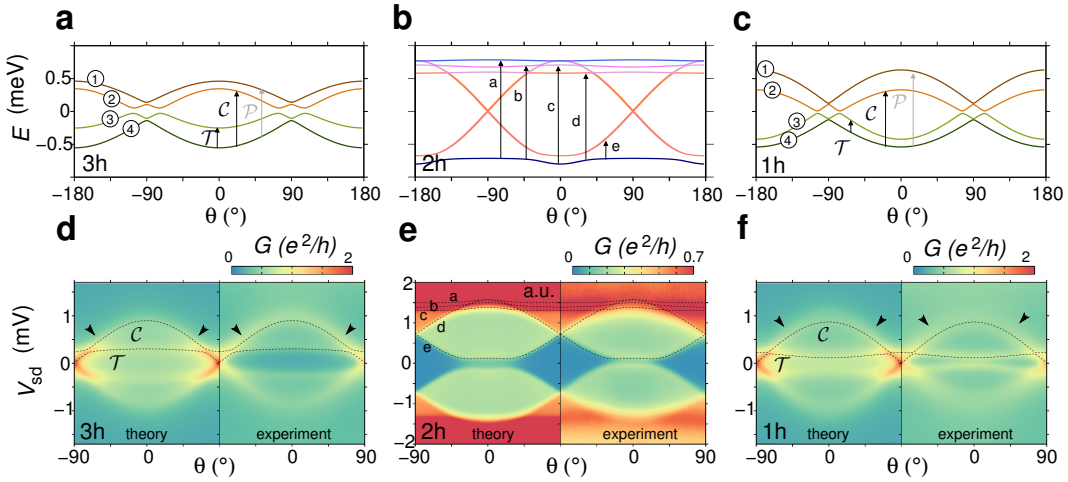

Supplementary Figure 5: Dependence on magnetic field orientation. Angular dependence of the energy spectrum and $\mathrm{d}I/\mathrm{d}V$ characteristics for negative gate voltages in the hole sector (shell N_h). **a-c,** Calculated energy level spectrum at fixed magnetic field, as a function of the angle θ between tube axis and the direction of the magnetic field. **d-f,** Corresponding as-measured (right hand side) and calculated differential conductance maps (left hand side) in the hole regime with respective hole fillings 3h, 2h and 1h (from left to right). The missing $\mathcal{P}$ resonances are indicated by arrows. The panels a)-f) correspond to an applied magnetic field of 0.8 Tesla.

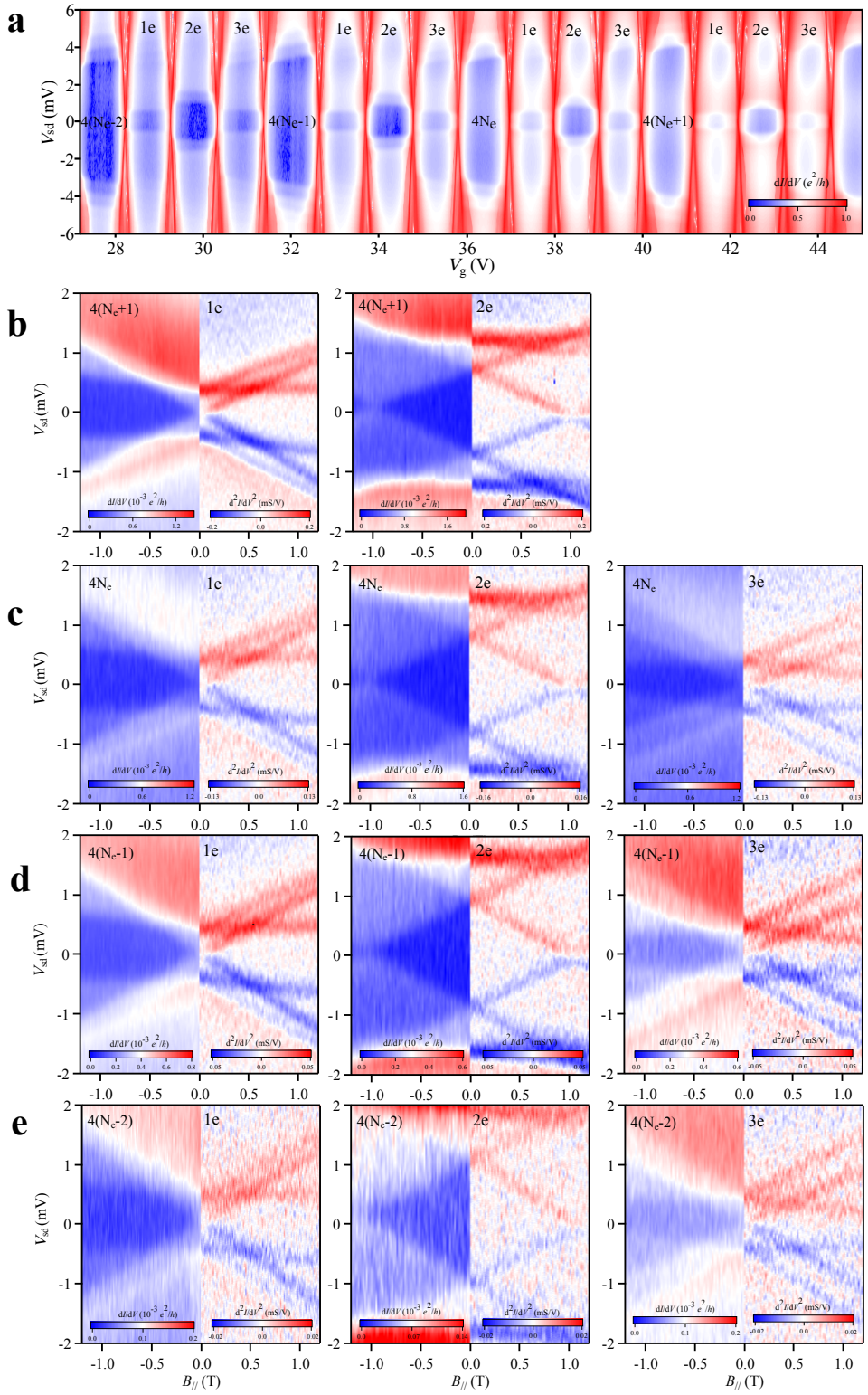

Supplementary Figure 6: Magnetotransport data in the cotunneling regime for different electron quadruplets. **a,** As-measured $\mathrm{d}I/\mathrm{d}V$ stability diagram at $B_{\parallel}$=0, representing the successive filling of up to four consecutive electron shells. The data discussed in the main text correspond to the quadruplet N_e with $4N_\mathrm{e}$ total electrons in the conduction band. **b-e,** Magnetotransport measurements of the 1e, 2e and 3e charge states (from left to right) for electrons in the quadruplets N_e+1 (b), N_e (c), $N_\mathrm{e}-1$ (d) and $N_\mathrm{e}-2$ (e), as a function of V_{sd} and $B_{\parallel}$. In each panel (b-e), we plotted both the experimental $\mathrm{d}I/\mathrm{d}V$ ($B_{\parallel}<0$) and its numerical derivative $\mathrm{d}^2I/\mathrm{d}V^2$ ($B_{\parallel}>0$). We notice here the extreme qualitative similarity of the magnetotransport curves, highlighting the robustness of the energy level spectrum, reproducible for several electron quartets.

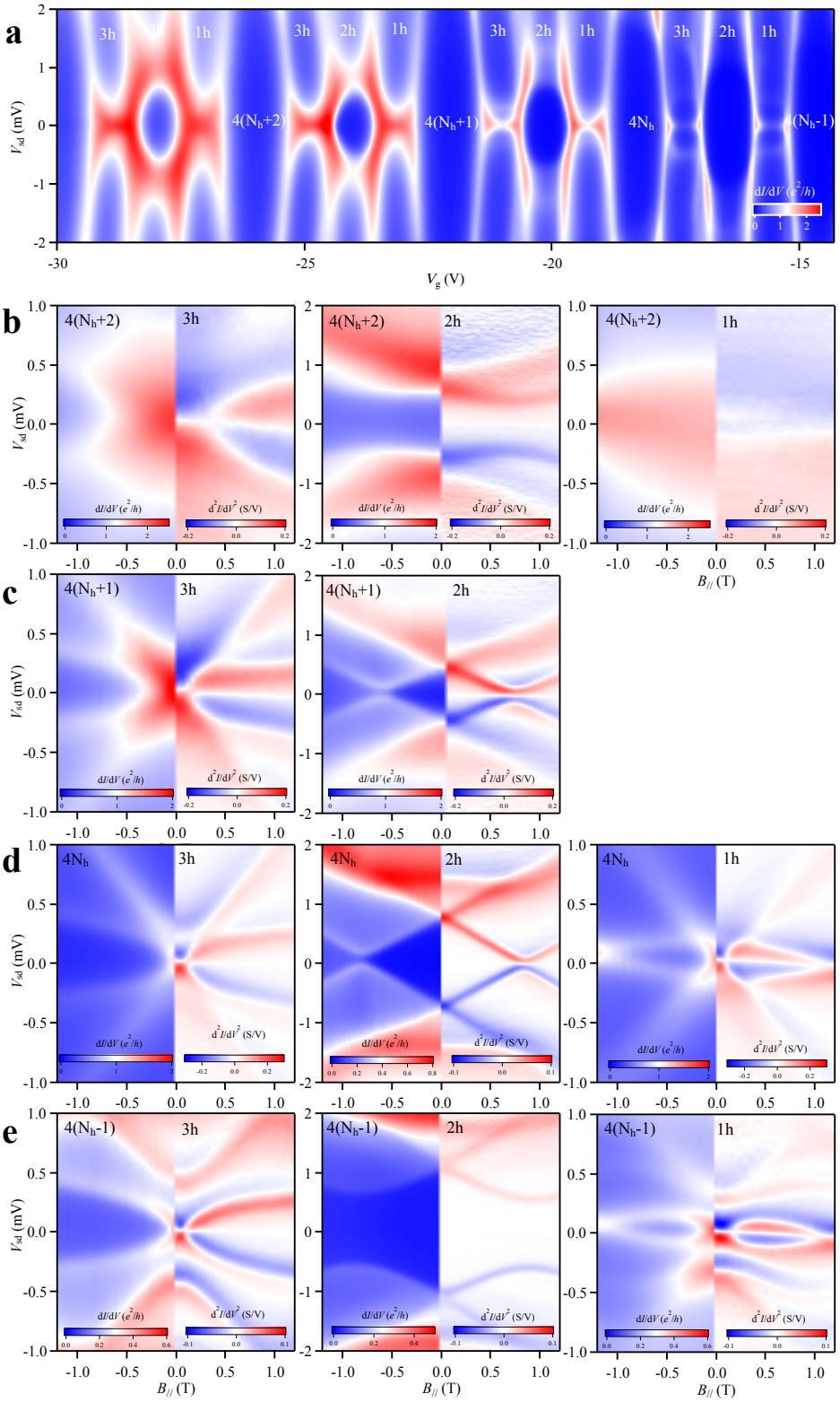

Supplementary Figure 7: Magnetotransport data for different hole quartets. **a,** As-measured $\mathrm{d}I/\mathrm{d}V$ stability diagram at $B_{\parallel}$=0, representing the successive filling of up to four consecutive hole quadruplets. The data discussed in the main text correspond to the hole quartet N_{h}. **b-e,** Magnetotransport measurements of the 3h, 2h and 1h charge states (from left to right) for hole shells N_{h}+2 (b), N_{h}+1 (c), N_{h} (d) and N_{h}-1 (e), as a function of V_{sd} and $B_{\parallel}$. In each panel (b-e), we plotted both $\mathrm{d}I/\mathrm{d}V$ ($B_{\parallel} < 0$) and $\mathrm{d}^2I/\mathrm{d}V^2$ ($B_{\parallel} > 0$) for direct comparison of both representations. By applying more negative gate voltage (shells N_{h}+1 and N_{h}+2), Kondo correlations are strengthened and the system approaches more and more the $SU(4)$ Kondo regime. For all quadruplets similar conclusions regarding the absence of $\mathcal{P}$ resonances in the Kondo regime can be drawn.

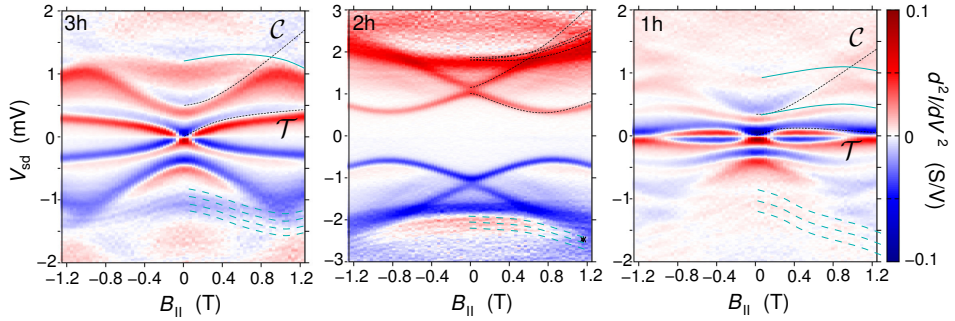

Supplementary Figure 8: Magnetotransport curves for the N_h-1 hole quartet with superposed excitation spectrum lines. Similar to the N_h quadruplet (cf. Fig. 2 of main manuscript), an analysis of the excitation spectrum allows us to identify the low energy $\mathcal{T}$ and $\mathcal{C}$ resonances at 1h and 3h filling. Additional harmonic excitations are also seen, which are not captured by our model Hamiltonian, for all hole fillings (dashed and solid lines).

Supplementary Tables

shell		Δ_{SO}(meV)	$\Delta_{\mathrm{KK'}}$(meV)	μ_{orb}(meV T^{-1})	J(meV)
electrons	$N_{\mathrm{e}}+1$	-0.40	0.04	0.37	-1.05
	N_{e}	-0.40	0.04	0.40	-1.30
	$N_{\mathrm{e}}-1$	-0.40	0.04	0.45 (1e, 3e), 0.32 (2e)	-1.00
	$N_{\mathrm{e}}-2$	-0.42	0.04	0.48	-1.80
holes	N_{h}+2	-0.21	0.30 (2h), 0.35 (3h)	0.43	-1.10
	N_{h}+1	-0.21	0.08	0.48	-1.10
	N_{h}	-0.21	0.08	0.55 (1h), 0.51 (2h, 3h)	-1.30
	$N_{\mathrm{h}}-1$	-0.21 (1h, 2h), -0.27 (3h)	0.27 (1h), 0.38 (2h, 3h)	0.70 (1h), 0.53 (2h), 0.60 (3h)	-1.65

Supplementary Table 1. The parameters used to fit the transport spectra of the CNT at various shells and filling numbers. The experimental data show an offset in V_{sd} of 0.28 meV(0.12 meV) and are tilted in the magnetic field by -0.06 meV T^{-1} (-0.05 meV T^{-1}) at the electron(hole) side. The hole side has an offset of the magnetic field of 0.06 T.

Supplementary Methods

The total Hamiltonian

In this section we discuss our theoretical modeling of the CNT-leads complex. A scanning electron microscopy of a device similar to the one used in the experiment is shown in the Supplementary Figure 1. In order to capture Coulomb blockade and Kondo physics, a segment of the CNT forming the quantum dot is assumed to be weakly coupled by a tunneling Hamiltonian to biased source (s) and drain (d) leads. The model Hamiltonian is then given by

$$\hat{H}_{\rm tot} = \hat{H}_{\rm CNT} + \hat{H}_{\rm tun} + \hat{H}_{\rm L}, \tag{1}$$

where $\hat{H}_{\rm CNT}$ is the Hamiltonian of the isolated CNT reported in Eq. (2) of the Methods. In particular, its single particle part $\hat{H}_0 = \hat{H}_{\rm d} + \hat{H}_{\rm KK'} + \hat{H}_{\rm SO} + \hat{H}_{\rm B}$ is diagonal in the Kramers basis spanned by the quadruplet $\{|i\rangle\}$, $i = 1, 2, 3, 4$ (shown in Fig. 1b of the main manuscript). Finally, $\hat{H}_{\rm tun}$ and $\hat{H}_{\rm L}$ are the tunneling and leads Hamiltonians, respectively. In what follows a diagonal tunneling coupling is assumed for the tunneling Hamiltonian in the Kramers basis:

$$\hat{H}_{\rm tun} = \sum_{l={\rm s,d}} \sum_{k,i} (T_{lki} \hat{c}^\dagger_{lki} \hat{d}_i + h.c.), \tag{2}$$

with k an index describing a continuum of modes in the leads. As suggested by the Supplementary Figure 1, we assume that the dot is a segment of the CNT and that the Kramers index i is conserved during the tunneling. To this Hamiltonian the coupling constants $\Gamma_{li} \equiv 2\pi\rho_l(\varepsilon_{\rm F})|T_{lki}|^2$ are associated, where $\rho_l(\varepsilon_{\rm F})$ is the density of states of lead l at the Fermi energy, and only a dependence on the lead l and Kramers index i has been retained in the tunneling coupling T_{lki}. In absence of SOC, valley mixing and exchange interaction the total Hamiltonian is $SU(4)$ invariant when all the couplings related to the lead l are equal: $\Gamma_{li} = \Gamma_l$ [1, 2], while the symmetry becomes $SU(2)\otimes SU(2)$ when only the rates within a Kramers channel are the same [3]. Finite valley scattering and SOC also reduce the symmetry to $SU(2)\otimes\ SU(2)$ [4, 5]. We assumed equal couplings within the Kramers channels $\Gamma_{l1} = \Gamma_{l2} = \Gamma_{l\rm u}$, $\Gamma_{l3} = \Gamma_{l4} = \Gamma_{l\rm d}$ in the DM-NRG simulations, and equal rates, $\Gamma_{l\rm u} = \Gamma_{l\rm d} = \Gamma_l = \Gamma$ for the Keldysh effective action (KEA) case.

An additional exchange coupling further breaks the $SU(2)$ symmetries in the 2h valley. For our DM-NRG calculations in the Kondo regime we have neglected the exchange coupling J. Its inclusion would have been possible but at the expense of a significant increase in the computational cost, due to the reduced symmetry. Likewise J was not included in the KEA.

Supplementary Notes

Supplementary Note 1. Impurity entropy and specific heat

One outcome of the experiment is that Kondo correlations, leading to the formation of the Kondo singlets, persist also at the finite temperature of the experiment. We notice that the mixing chamber temperature $T_{\rm exp} = 30$ mK sets a lower bound to the actual experimental temperature. Given the uncertainty in determining the experimental Kondo temperature from the width of the zero bias peak of the differential conductance (cf. Supplementary Figure 2 and related discussion), we can only give a range for the ratio $T/T_{\rm K}$ in the experiment. According to our DM-NRG calculations for the linear conductance (cf. Fig. 1h of the main manuscript), it lies in the range $0.1 < T/T_{\rm K} < 1$. To further quantify the impact of thermal fluctuations, we have performed additional calculations of the impurity entropy and specific heat. Thermodynamic entropies $S(T) = k_{\rm B} \ln Z(T) + \langle \hat{H} \rangle / T$, associated to a given Hamiltonian $\hat{H}$, are easily accessible through DM-NRG schemes [6–9]. Here Z is the partition function and $\langle ... \rangle$ the associated thermal average. Specifically, we have calculated the conditional entropy $S_{\rm CNT}(T) = S_{\rm tot}(T) - S_{\rm L}(T)$ as a function of temperature. This so called impurity entropy is zero if the total system is in a pure singlet ground state (degeneracy one). At finite temperature also excited states become accessible and the conditional entropy $S_{\rm CNT}(T)$ grows. As seen in the Supplementary Figure 2, it grows very slowly in the Fermi liquid regime which persists up to temperatures of the order of $10^{-2} T_{\rm K}$. At higher temperatures the growth is faster but the behavior is still universal until $T \approx T_{\rm K}$. At even larger temperatures nonuniversal features are seen, like a shoulder at temperatures of the order of $\Delta/k_{\rm B}$. At very high temperatures the CNT is in a fully incoherent mixture, where all of its Fock states are occupied. Correspondingly, the entropy shows a plateau with value $S_{\rm CNT}/k_{\rm B} = \log(16)$. A second thermodynamic quantity of interest is the specfic heat $C = T\partial S/\partial T$. It can be calculated numerically within the Budapest code from the relation $C(T)/k_{\rm B} = \beta^2 \langle (\hat{H} - \langle \hat{H} \rangle)^2 \rangle$ [8]. The impurity specific heat $C_{\rm CNT} = C_{\rm tot} - C_{\rm L}$ is reported in the bottom panel of Fig. S2. Minima of $C_{\rm CNT}$ are clearly resolved in correspondence of the position of the shoulders and of the plateau of $S_{\rm CNT}$. The results shown in the Supplementary Figure 2 have been obtained using a constant number of multiplets $N_{\rm kept} = 8192$ (fixing the initial discarding iteration to $m_0 = 2$) and averaged the results, according to Ref. [6], over $n_z = 4$ simulations with $z = 1/4, 1/2, 3/4, 1$ and the discretization parameter $\Lambda = 5$.

Supplementary Note 2. Transport regimes

All calculations shown in the main part of the paper have been performed using the total Hamiltonian (1) with a different set of parameters and computational techniques depending on the transport regime. In the experiment several electron and hole longitudinal modes can be investigated by sweeping the gate voltage. According to the notation used in the Supplementary Figures 4 and 5, the data shown in the main text refer to the conduction quadruplet $N_{\rm e}$ and to the valence quadruplet $N_{\rm h}$, respectively. As shown in Table 1 of the main manuscript, the parameters $\Delta_{\rm SO}$, $\Delta_{\rm KK'}$ and $\mu_{\rm orb}$ entering the single-particle Hamiltonian $\hat{H}_0$ do not differ much for the electron and hole sectors. However, the charging energy U greatly vary in the two regimes (but not the couplings Γ_{li}), which requires the use of different transport methods.

Weak coupling regime. At positive gate voltages (electron regime) transport is dominated by sequential and cotunneling processes, as clearly observed in the experimental transport data of Fig. 1c, 1e. This indicates large charging energies U and a parameter regime where Kondo correlations are not relevant yet. A perturbative calculation in the couplings Γ_{li} is expected to qualitatively capture the dominant sequential tunneling and cotunneling mechanisms [10]. For our transport calculations we have followed a reduced matrix density approach which retains all tunneling processes up to second order in the couplings Γ_{li} [11]. As seen from the comparison shown in Figs. 1,2 of the main manuscript, this approach indeed well captures all the inelastic features observed in the experiment in the whole electron sector, as well as for the 2h case. Due to its perturbative nature though, it fails to account for a broadening of the conductance traces being larger than the nominal experimental temperature (a thermal broadening is expected from the PT), see Fig. 1e. This large broadening signals that also higher order charge fluctutation processes might influence transport, yielding a width governed by Γ rather than by the temperature [12–15]. From the experimental curves we extract an average half width at half maximum of 0.15 meV.

In the perturbative simulations, much smaller values of the tunneling coupling had to be choosen in order to fullfill the theoretical requirement $\Gamma \ll k_{\rm B}T$ for the application of the PT. Since the calculations also include an exchange splitting, it was convenient in this regime to work in the $\{|\tau,\sigma\rangle\}$ basis. Besides the parameters shown in Table 1 of the main manuscript, the additional parameters used in the simulations are $T = 232$ mK, and symmetric leads with tunneling couplings $\Gamma_{K,\uparrow} = \Gamma_{K',\downarrow} = 0.06\mu$eV, $\Gamma_{K,\downarrow} = \Gamma_{K',\uparrow} = 0.047\mu$eV.

Strong coupling regime. The appearance of Kondo ridges in valleys with odd hole occupations indicates a regime of strong correlations which requires a nonperturbative treatment in the couplings Γ_{li}.

To quantitatively analyze the linear regime, we have performed numerical DM-NRG calculations using the open access Budapest code [16]. We have assumed a broken $SU(4)$ symmetry, and used the generators of the $SU(2)$ symmetries associated to the upper and lower Kramers channels along the lines explained in Sec. 2 of [5]. Such calculations, performed at $T = 30$ mK and with the parameters of the isolated CNT given in Table 1 of the Methods, enabled us in particular to estimate the coupling to the leads and the charging energy U. We allow for an asymmetry $\alpha = 4\tan\gamma/(1+\tan\gamma)^2$ between source (s) and drain (d) leads, with $\tan\gamma = \Gamma_{{\rm d}i}/\Gamma_{{\rm s}i}$ (which fixes the height of the 2-3 peak in the gate trace of Fig. 1f). The fit in Fig. 1f yields: $\alpha = 0.9$ and $\Gamma_{\rm su} = 0.50$ meV, $\Gamma_{\rm sd} = 0.64$ meV for the u/d Kramers channels coupled to the s-lead. Furthermore, we find $U = 4.7$ meV, which in turn yields the Kondo temperatures $T_{\rm K}(\Delta)$, as shown in Fig. 1h. Notice that a different choice of the temperature T would have implied a different set of parameters for fitting to the experiment, and hence also different Kondo temperatures. Nevertheless, we are confident that our estimate of the ratio $T/T_{\rm K}$ is close to the experimental one, as is this ratio, for example, which determines how pronounced are the minima of the linear conductance in valley 1h and 3h.

In order to describe also finite bias effects, and hence account for the inelastic transitions, one has to resort to transport approaches to the Kondo effect valid out of equilibrium. To this extent we have used the Keldysh effective action (KEA) approach, recently developed by some of us [17, 18]. The KEA is based on a slave boson field integral formulation, where a truncation of the effective action to terms quadratic in the slave boson fields enables us to evaluate the tunneling density of state of the Kondo quantum dot in analytic form. Due to such truncation, some cotunneling terms which become relevant at high bias voltage or large magnetic fields are neglected. As such, the KEA is expected to quantitatively describe the positions of the inelastic Kondo peaks at finite bias and magnetic field, but only qualitatively their shapes [18].
For the KEA calculations symmetric and equal couplings $\Gamma_{li} = \Gamma$ were assumed, an infinite charging energy U and no exchange coupling. This parameter choice necessarily yields a different Kondo temperature than in the experiments, which e.g. naturally have a finite charging energy and different couplings $\Gamma_{l\rm u}$ and $\Gamma_{l\rm d}$. Moreover, due to the choice of infinite U, our calculations well describe Kondo behavior when the effects of the fluctuations to states with double occupancy can be neglected, i.e. away from the middle of the diamonds with one or three holes. The experimental curves shown in the Figs. 2 and 4 of the main text, however, correspond to gate voltages in the middle of the 1h and 3h diamonds. Nevertheless, due to the universal scaling properties of the differential conductance in the Kondo regime, the predictions of the KEA theory can become quantitative when both the experimental data and the theoretical curves are scaled by

the respective Kondo voltage [19], or by an energy scale proportional to it (cf. next Supplementary Note 4), as long as only universal features are relevant.

Supplementary Note 3. Differential conductance traces

Experimental bias traces are compared to (zero temperature) KEA predictions in the Supplementary Figure 3. An overall qualitative agreement between theoretical and experimental prediction is observed. A quantitative agreement is found regarding the position of the $\mathcal{T}$ and $\mathcal{C}$ resonances, see e.g. panels a) and b). Clearly, the $\mathcal{P}$ resonance, whose expected position is indicated by vertical lines, is not resolved at low fields. Signatures of the re-emergence of such transition are observed at fields of the order of 0.9 T, a shoulder in panels c) and d). However, higher magnetic fields, not accessible to the experiment, would be necessary to track the evolution of this shoulder at even higher bias voltages. In our calculations the temperature was set to zero and we have choosen a source drain voltage V^* such that $G(T=0, V=V^*) = 0.8G(T=0, V=0)$. At this voltage, the dynamics is still universal and V^* is proportional to the Kondo voltage. E.g. for our symmetric set-up with $\Gamma_{li} = \Gamma$ we find $V^* = 0.41V_{\rm K}$ with $V_{\rm K} = k_{\rm B}T_{\rm K}/e$. We have also checked the evolution of this relation at finite temperatures. For temperatures $T = 0.13\Delta/k_{\rm B}$, similar to the experiment, we found $G(T, V=V^{**}) = 0.8G(T, V=0)$ with $V^{**} = 0.59V_{\rm K}$. To allow for comparison, the experimental data are scaled by a bias voltage $V^*_{\rm exp} = 0.0842$ mV for which $G(T, V=V^*_{\rm exp}) = 0.8G(T, V=0)$ for both the 1h and 3h valleys.

Supplementary Note 4. Differential conductance stability diagrams

This section provides additional experimental data, with their theoretical analysis, complementary to the ones presented in the main text. The Supplementary Figure 4 reports the as-measured and simulated magnetospectra of the differential conductance $\mathrm{d}I/\mathrm{d}V$, used to infer the current second derivative $\mathrm{d}^2I/\mathrm{d}V^2$ plots in Fig. 2 of the main text by numerical derivation, in both cotunneling and Kondo regimes. The inflexion points of the differential conductance steps (Supplementary Figure 4), in the cotunnelling regime, thus translate into extrema in the $\mathrm{d}^2I/\mathrm{d}V^2$ (Fig. 2). Analogously, maxima of the differential conductance at the Kondo resonance peaks appear as zeros of the $\mathrm{d}^2I/\mathrm{d}V^2$. In the Supplementary Figure 5 we provide the differential conductance version of the energy spectrum angular dependence (cf. Fig. 4 main text), including also the 2h valley. The same conclusions regarding the nature of the relevant inelastic resonances can be drawn, as obtained from the inspection of the current second derivative plots of the main text, used because of enhanced eye visibility of the excitation spectra.

Supplementary Note 5. Magnetospectrum of other quartets

Up to now, we only considered one selected quartet for holes and electrons lying respectively in the CNT valence and conduction bands. Here we show that comparable conclusions regarding the suppression of $\mathcal{P}$ channels due to Kondo screening can be drawn for other quartets, showing the generality of the analysis depicted in the main text.

In the cotunneling regime, observed for electrons lying in the conduction band, the CNT transport characteristics has been thoroughly investigated by magnetospectroscopy for different electron fillings. The Supplementary Figure 6 depicts part of the measurements, which display the same qualitative behavior as the studies in Fig. 2 of the main text.

Analogously, the strongly correlated regime has been investigated for various hole shell numbers (see additional data in the Supplementary Figure 7). By tuning the gate voltage it is possible to follow the system evolution over the full transition from the $SU(4)$ to $SU(2)$ transport regimes in a controllable way [20, 21]. In the present study, we are more interested in checking the robustness of the suppression of the $\mathcal{P}$ lines by inspecting the magnetic field evolution in different quadruplets. In general, neither in the quadruplets with stronger Kondo correlations (shells $N_{\rm h}+1$ and $N_{\rm h}+2$) nor in the one with a weaker Kondo effect (shell $N_{\rm h}-1$), the $\mathcal{P}$ transition can be resolved from an analysis of the excitation spectrum, as exemplarily shown in the Supplementary Figure 8. Notice that due to gate voltage instability we do not report on the magnetic field evolution in the 1h valley of the $N_{\rm h}$ +1 and $N_{\rm h}$+2 quadruplets.

Supplementary References

[1] Choi, M.-S., López, R. & Aguado, R. SU(4) Kondo effect in carbon nanotubes. *Phys. Rev. Lett.* **95**, 067204 (2005).

[2] Anders, F., Logan, D., Galpin, M. & Finkelstein, G. Zero-bias conductance in carbon nanotube quantum dots. *Phys. Rev. Lett.* **100**, 086809 (2008).

[3] Lim, J. S., Choi, M.-S., Choi, M. Y., López, R. & Aguado, R. Kondo effects in carbon nanotubes: From SU(4) to SU(2) symmetry. *Phys. Rev. B* **74**, 205119 (2006).

[4] Galpin, M. R., Jayatilaka, F. W., Logan, D. E. & Anders, F. B. Interplay between Kondo physics and spin-orbit coupling in carbon nanotube quantum dots. *Phys. Rev. B* **81**, 075437 (2010).

[5] Mantelli, D., Moca, C., Zaránd, G. & Grifoni, M. Kondo effect in a carbon nanotube with spin-orbit interaction and valley mixing: A DM-NRG study. *Physica E* **77**, 180-190 (2016).

[6] Oliveira, Wanda C. & Oliveira, Luiz N. Generalized numerical renormalization-group method to calculate the thermodynamical properties of impurities in metals. *Phys. Rev. B* **49**, 11986 (1994).

[7] Merker, L., Weichselbaum, A.,& Costi, T. Full density-matrix numerical renormalization group calculations of impurity susceptibility and specific heat of the Anderson impurity model. *Phys. Rev. B* **86**, 075150 (2012).

[8] Merker, L., & Costi, T. Numerical renormalization group calculations of impurity internal energy and specific heat of quantum impurity models. *Phys. Rev. B* **86**, 075153 (2012).

[9] Filippone, M.,Moca, C.P., Zaránd, G., & Mora, C. Kondo temperature of SU(4) symmetric quantum dots. *Phys. Rev. B* **90**, 121406 (2014).

[10] Grabert, H. & Devoret editors, M. *Single charge tunneling* (Plenum Press, New York, 1992).

[11] Koller, S., Leinsje, M., Wegewijs, M. & Grifoni, M. Density operator approaches to transport through interacting quantum dots: Simplifications in fourth-order perturbation theory. *Phys. Rev. B* **82**, 235307 (2010).

[12] König, J., Schmid, J., Schoeller, H. & Schön, G. Transport through an Anderson quantum dot in the intermediate coupling regime. *Phys. Rev. B* **54**, 16820-16837 (1996).

[13] Pedersen, J. N. & Wacker, A. Tunneling through nanosystems: Combining broadening with many-particle states. *Phys. Rev. B* **72**, 195330 (2005).

[14] Kern, J. & Grifoni, M. Transport through an Anderson quantum dot in the intermediate coupling regime. *Eur. Phys. J. B* **86**, 384 (2013).

[15] Dirnaichner, A. *et al.* Transport across a carbon nanotube quantum dot contacted with ferromagnetic leads: Experiment and nonperturbative modeling. *Phys. Rev. B* **91**, 195402 (2015).

[16] Toth, A., Moca, C., Legeza, Ö. & Zaránd, G. Density matrix numerical renormalization group for non-Abelian symmetries. *Phys. Rev. B* **78**, 245109 (2008).

[17] Smirnov, S. & Grifoni, M. Keldysh effective action theory for universal physics in spin-1/2 Kondo dots. *Phys. Rev. B* **87**, 121302(R) (2013).

[18] Schmid, D. *et al.* Broken SU(4) symmetry in a Kondo-correlated quantum dot. *Phys. Rev. B* **91**, 155435 (2015).

[19] Kretinin, A. V., Shtrikman, H. & Mahalu, D. Universal line shape of the Kondo zero-bias anomaly in a quantum dot. *Phys. Rev. B* **85**, 201301(R) (2012).

[20] Makarovski, A., Zhukov, A., Liu, J. & Finkelstein, G. SU(2) and SU(4) Kondo effects in carbon nanotube quantum dots. *Phys. Rev. B* **75**, 241407 (2007).

[21] Cleuziou, J. P., N'Guyen, N. V., Florens, S. & Wernsdorfer, W. Interplay of the Kondo effect and strong spin-orbit coupling in multihole ultraclean carbon nanotubes. *Phys. Rev. Lett.* **111**, 136803 (2013).